








Underestimated accelerated Antarctic phytoplankton net primary production in winter over past decade from spaceborne LiDAR

Received: 9 May 2025

Accepted: 4 November 2025

Published online: 12 December 2025

 Check for updates

Peng Chen ^{1,2,8} ✉, Zhenhua Zhang ^{1,2,8}, Kelsey Bisson ³, Cédric Jamet ⁴, Paolo Di Girolamo⁵, Davide Dionisi ⁶, Yongxiang Hu ⁷, Siqi Zhang ^{1,2} ✉ & Delu Pan^{1,2}

The Southern Ocean's vital carbon sink is driven by phytoplankton Net Primary Production (NPP). Winter phytoplankton seed spring algal blooms and regulate nutrient cycling and ecosystem dynamics, yet Antarctic winter NPP remains poorly constrained due to limited in situ data and passive satellite sensor challenges in low-light, ice-covered conditions. Here, we leverage spaceborne LiDAR (CALIOP), analyzing 16 years of data (16,236 tracks spanning 2006-2023), to reveal a significant, previously underestimated rise in winter NPP, increasing by $-2.2 \text{ Tg C yr}^{-1}$ ($P < 0.01$). Enhanced coverage with CALIOP boosts ice-free sea observations from 12.5% to 80.7%, exposing pronounced NPP gains in the seasonal sea-ice zone, notably the Weddell and Ross Seas, driven by declining sea ice, greater light penetration, and nutrient mixing. These shifts, modulated by climate modes like the Southern Annular Mode and El Niño-Southern Oscillation, highlight the Southern Ocean's escalating role in global carbon dynamics. Integrating winter NPP into carbon models is essential to refine projections of polar carbon sequestration under climate change.

The Southern Ocean plays a pivotal role in Earth's climate system, acting as a major carbon sink¹⁻³ because of its high rates of phytoplankton net primary production (NPP). NPP refers to the conversion of carbon dioxide (CO₂) into organic carbon through photosynthesis, which is then transferred through the marine food web or sequestered in deep ocean waters, helping to store carbon and mitigate climate change⁴. The sensitivity of Southern Ocean phytoplankton to environmental changes, including ocean warming, wind speeds, limited

iron contents, and sea ice melting, makes the Southern Ocean a critical area for studying the impacts of climate change on marine ecosystems and global biogeochemistry⁵⁻⁷.

Recent studies have highlighted the significant influence of climate change on Southern Ocean phytoplankton, with rising temperatures, shrinking sea ice, and alterations in ocean circulation affecting their distribution and production. Specifically, a warmer ocean and atmosphere^{8,9} and sea ice retreat¹⁰⁻¹² are reshaping the

¹State Key Laboratory of Satellite Ocean Environment Dynamics, Second Institute of Oceanography, Ministry of Natural Resources, Hangzhou, China.

²Southern Marine Science and Engineering Guangdong Laboratory (Guangzhou), Nansha District, Guangzhou, China. ³Department of Botany and Plant Pathology, Oregon State University, Corvallis, OR, USA. ⁴Université Littoral Côte d'Opale, CNRS, Université Lille, IRD, Laboratoire d'Océanologie et de Géosciences (LOG), Wimereux, France. ⁵Dipartimento di Scienze della Salute, Università degli Studi della Basilicata, Via dell'Ateneo Lucano n.10, Potenza, Italy. ⁶Institute of Marine Sciences (ISMAR), Italian National Research Council (CNR), Rome - Tor Vergata, Rome, Italy. ⁷NASA Langley Research Center, Hampton, VA, USA. ⁸These authors contributed equally: Peng Chen, Zhenhua Zhang. ✉e-mail: chenp@sio.org.cn; sqzhang@sio.org.cn

timing and magnitude of phytoplankton blooms by influencing the wind strength, nutrient availability, light conditions^{3,14} and mixed layer depth^{15–17}, which are factors that affect phytoplankton blooms. These regional shifts are often modulated by the Southern Annular Mode (SAM), the dominant climate pattern in the Southern Hemisphere. A positive SAM trend has been shown to influence phytoplankton communities and production by altering physical drivers like mixed layer depth, light availability, and sea ice cover^{18–20}. Notably, a recent intensification of the SAM since 2010 has been linked to increased phytoplankton biomass and longer blooms in the West Antarctic Peninsula²¹. These shifts in the timing and magnitude of phytoplankton blooms are particularly evident in austral summer, when phytoplankton blooms grow in magnitude but terminate earlier compared to previous decades, with significant trends in bloom initiation and termination observed over the past 25 years (1998–2022)⁵. In the marginal ice zone to the west of the Antarctic Peninsula, climate change is causing the timing of phytoplankton blooms to shift, with increased chlorophyll-*a* concentrations (*Chla*) in fall and a decrease in bloom intensity in spring²². A “greening” of *Chla* in the Southern Ocean has been observed²³, similar to the climate-driven trends observed in low-latitude regions²⁴, where the timing and intensity of phytoplankton blooms have shifted as the ocean has been subjected to warming, anthropogenic nutrient inputs²⁵, and acidification²⁶. Over the past two to three decades, long-term increases in *Chla*, with regional differences in phytoplankton blooms, have also been observed via satellite-based observations^{5,27}. However, in these observations, the critical role of wintertime production, which enables early-season phytoplankton growth under low-light conditions that support biomass buildup and sustain the spring bloom^{28,29}, is often overlooked. This is primarily because the passive ocean color remote sensing techniques depend on sunlight, and existing approaches typically cannot capture data under low-light conditions^{30,31}. Additionally, the presence of white caps—foam-covered wave crests formed by wind—significantly increases surface reflectance, particularly during winter storms, further complicating satellite observations³².

A significant gap in the current understanding of NPP in the Southern Ocean arises from this seasonal data limitation. Satellite-based studies and shipborne observations have focused mostly on summer^{33,34}, leaving the Antarctic winter months (June to August) underrepresented. While biogeochemical (BGC)-Argo floats collect some data in winter²⁹, their sparse coverage makes continuous long-term observations challenging. The coverage rate of ocean color remote sensing data, which are commonly used to estimate NPP^{35,36}, in ice-free sea areas of the Antarctic in winter is less than 15%, especially in June and July, when the coverage rate is less than 1% (Fig. S1). However, phytoplankton can still survive underneath sea ice even under extremely low-light conditions, which are typical of the polar night^{29,37–39}—a period in polar regions when the sun does not rise above the horizon for weeks or months.

To address this critical gap, we use spaceborne light detection and ranging (LiDAR) active remote sensing technology, which has already proven powerful in polar ocean detection because this technology does not require sunlight and can provide extensive spatial coverage^{31,40–44}. The effective coverage rate of cloud-aerosol LiDAR with orthogonal polarization (CALIOP) in Antarctic winter is 6 to 7 times greater than that of moderate resolution imaging spectroradiometer (MODIS), and the use of CALIOP can increase the effective coverage area from 12.5% to 80.7% (Fig. S1). Even in June, the coverage rate of CALIOP is more than half of the sea ice-free ocean area, and the coverage rates in July and August are both greater than 80%. However, few studies used the spaceborne LiDAR data to retrieve chlorophyll concentration or explore the dynamics of polar primary production. In this study, CALIOP technology is utilized to retrieve winter phytoplankton data, offering a more complete picture of long-term trends,

full seasonal cycles and potential drivers of Antarctic phytoplankton production.

The aim of this study is to address the critical gap in Antarctic NPP by utilizing enhanced satellite-based techniques, filling the void of winter observations. By incorporating CALIOP data from both the winter and summer months, we generate a comprehensive monthly dataset using spaceborne LiDAR, revealing a significant increase in Antarctic winter NPP over the past decade. The study area covers the Antarctic continental shelf and the seasonal sea-ice zone (SSIZ), the area within the temporally average extent of sea ice, which is bounded by the gray solid line in Fig. S1. This area is chosen as the focus of this study because the Antarctic shelf and its surrounding coastal areas are highly ecologically important, serving as habitats for all penguin species in Antarctica, and this area is characterized by high phytoplankton production⁴⁵. In this work, we present insights into the seasonal variations in primary production, identify long-term trends and key drivers, and attain a more complete understanding of the mechanisms shaping NPP in this critical region. The results of our research complement existing data by covering previously unobserved NPP in winter months, and the drivers of observed changes are quantitatively analyzed, illuminating how climate change impacts the Southern Ocean’s primary production. By filling a significant gap in wintertime Antarctic NPP data and analyzing the drivers of observed changes, this study offers valuable insights into how climate change impacts primary production in the Southern Ocean.

Results and discussion

Underestimated substantial increase in Antarctic winter NPP

To determine the Antarctic winter NPP, we first compared the variability in NPP from CALIOP with that from MODIS. To derive NPP from CALIOP data, we used the two-branch-two-step (TBTS) deep learning model to retrieve *Chla*, backscattering coefficient (b_{bp}), and attenuation coefficient (K_d), followed by the application of the carbon-based productivity model (CbPM) to estimate NPP, whereas MODIS-derived NPP data were accessible from <http://orca.science.oregonstate.edu/1080.by.2160.monthly.hdf.cbpm2.m.php>. Antarctic winter NPP, defined as the sum of June, July, and August NPP, has exhibited significant spatial variability and a notable increase from 2007 to 2022 (Fig. 1). The CALIOP-derived climatological winter NPP shows high production concentrated along the edge of the ice in the SSIZ (Fig. 1a), where sea-ice retreat creates favorable conditions for the growth of phytoplankton⁴⁶ by allowing more sunlight to penetrate the surface waters and increasing the availability of nutrients. In comparison, although the MODIS-derived NPP (Fig. 1b), captures similar spatial patterns, production levels are underestimated because of the limitations of this passive remote sensing technique under low-light winter conditions.

To further explore the patterns of NPP change, we examined the spatial distribution of NPP variations across different regions (Fig. 1c, d). This analysis reveals distinct patterns of both increases and decreases in winter NPP. CALIOP-derived rates of NPP change (Fig. 1c) show widespread increases in production along the SSIZ, particularly in the Weddell Sea, Ross Sea, and parts of the Indian Ocean sector. Consistent increases in production are observed in these regions, likely driven by thinning sea ice, as shown in Figs. S2 and S3, as well as increased light penetration and episodic nutrient mixings. However, areas of NPP decline are also evident, such as in the Bellingshausen Sea and the eastern Amundsen Sea, where environmental factors such as unfavorable ice dynamics—like increased sea ice concentration, which can limit light penetration and hinder phytoplankton growth—along with limited nutrient access, as shown in Fig. S3, likely contributed to these reductions. Compared with the CALIOP observations, the MODIS-derived rates of NPP change (Fig. 1d) reveal weaker and more spatially limited trends, with substantial increases and decreases observed in fewer areas. These differences highlight the advantages of

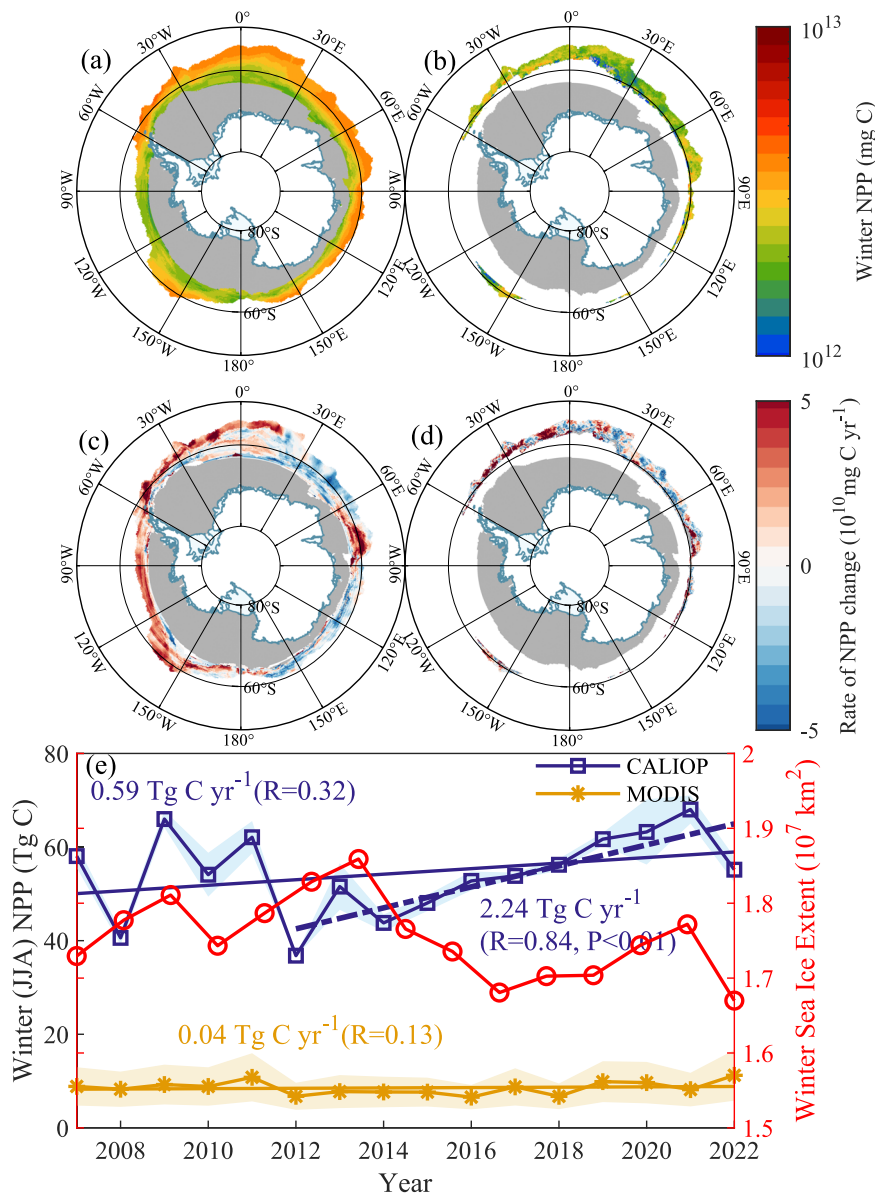


Fig. 1 | Spatial and temporal variability in Antarctic winter net primary production (NPP). **a, c** CALIOP-derived annual mean winter NPP distributions and winter rates of NPP change (2007–2022), respectively. **b, d** MODIS-derived annual mean winter (June–July–August (JJA)) NPP distributions and winter rates of NPP change (2007–2022), respectively. Gray represents the permanent ice zone in winter. **e** Interannual trends in winter Antarctic NPP. The blue squares and

yellow–orange stars represent the CALIOP and MODIS-Aqua results, respectively. The solid green and yellow–orange lines represent the CALIOP and MODIS linear fits, respectively, from 2007 to 2020. The dotted green line represents CALIOP fit from 2012 to 2022. The green and yellow–orange data and associated lines correspond to the left vertical axis. The red circles show the average extent of sea ice in winter, corresponding to the right vertical axis.

using CALIOP data for a more detailed and comprehensive assessment of NPP changes, especially in regions where sea-ice dynamics play a critical role in primary production. The ability to capture finer spatial variability in NPP is a key strength of the CALIOP-based approach over the MODIS data.

Temporal trends reveal a marked increase in winter NPP over the study period (Fig. 1e). From 2007 to 2022, the annual mean CALIOP-derived winter NPP is 54.5 ± 8.9 Tg C, which is six times greater than the MODIS-derived NPP (8.5 ± 1.4 Tg C). A sharp acceleration in NPP is observed in the later years (2012–2022), with an annual increase of 2.24 Tg C yr⁻¹ ($R = 0.84$, $P < 0.01$). This acceleration corresponds to ongoing reductions in the extent of winter sea ice, as shown by the steady decline in winter sea ice extent (Fig. 1e, red circles). In contrast, the MODIS-derived NPP shows minimal changes over the same period, underscoring the importance of active remote sensing technologies

for observing winter phytoplankton dynamics. Moreover, with the completion of CALIOP data collection, the annual pan-Antarctic (i.e., the entire Antarctic SSIZ) phytoplankton NPP calculated from 2007 to 2022 was 1022.8 ± 136.8 Tg C; without these data, the NPP estimated on the basis of MODIS data alone would be underestimated by nearly 15%, a substantial difference that suggests the importance of CALIOP (Fig. S4).

Next, in an effort to verify the increasing trend, several additional NPP models were investigated: the vertically generalized production model (VGPM), carbon, absorption, and fluorescence euphotic-resolving (CAFE) model, and Eppley model. These models were selected based on their ability to estimate NPP across different oceanographic conditions. Evaluating multiple models allows for a more robust validation of the increasing trend observed in winter NPP. The data from all four models VGPM, CbPM, CAFE, and Eppley indicate a

clear increase in polar winter NPP, with the most significant increase observed between 2012 and 2022. The CAFE model consistently estimates the highest NPP, followed by the VGPM and CbPM, whereas a more modest increase is obtained with the Eppley model (Fig. S5). These trends highlight the increasing production in the polar regions, particularly in winter. This finding aligns with the findings shown in Fig. 1e, emphasizing that the winter NPP in the Southern Ocean has increased substantially over the last decade.

Given that the CALIOP-derived results utilizes MODIS data for training, biases present in the MODIS data^{47,48} are likely to be propagated in the ensuing CALIOP outputs and affect the resulting CALIOP b_{pp} , $Chla$, and K_d predictions, which in turn affects the accuracy of NPP calculations. In addition, in-situ BGC-Argo data were used to validate CALIOP-derived NPP. A total of 125 Argo floats and 5131 observation profiles were deployed in the SSIZ from 2012 to 2023, with a seasonal distribution of 583 profiles in winter (June–August), 579 in spring, 1968 in summer, and 2001 in autumn. Fig. 2a illustrates the spatial distribution of these profiles by season. The Argo NPP rate values were derived by inputting the water parameters observed by the Argo floats into the CbPM model⁴⁹. To specifically assess our model's performance during the critical, under-sampled winter period, we compared our CALIOP NPP estimates exclusively against the wintertime Argo profiles (Fig. 2b). Despite the relative sparsity of in-situ winter data, this targeted validation reveals a good correlation providing confidence in our model's ability to retrieve NPP in the challenging low-light conditions of the polar winter. A comprehensive validation across all seasons, including individual plots for spring, summer, and autumn, is provided in Supplementary Fig. S11 for a complete performance assessment. Although there is some margin of error, the overall agreement validates the use of CALIOP data for monitoring primary production in polar regions, where in situ data are often limited.

Owing to the sparsity of the Argo data, we employ a $5^\circ \times 4^\circ$ grid system to organize the Argo data on a monthly basis spatially. We then analyzed the winter NPP trends in the Antarctic using these sparse BGC-Argo data. Fig. 2c shows a map of the spatial distribution of winter observation frequencies within a $5^\circ \times 4^\circ$ grid system, revealing stark disparities in data coverage across the Southern Ocean. While up to eight observations were obtained in some grids, vast areas remain poorly sampled, reflecting the logistical challenges of polar data collection. Fig. 2d quantifies this sparsity, showing that fewer than five winter observations were obtained in the majority of grids ($5^\circ \times 4^\circ$) in the 2012–2023 study period. Such limited coverage complicates robust temporal or spatial analyses of NPP. Fig. 2e shows the winter NPP calculated in the grid with the highest observation frequency, displaying a positive trend of winter NPP rate. Notably, this trend mirrors CALIOP-LiDAR satellite-derived NPP estimates, validating the consistency between in situ and remote sensing datasets. The alignment underscores the critical role of satellite technologies like CALIOP in bridging observational gaps, particularly in remote polar regions where traditional methods face limitations. Together, these results highlight both the challenges of relying on sparse Argo data and the value of integrating multiplatform approaches to advance understanding of Antarctic primary production dynamics.

Given that our CALIOP retrieval model was trained using MODIS data, it is important to address the potential for data dependency and validate our findings with an independent satellite sensor. To this end, we conducted an independent analysis using data from the Visible Infrared Imaging Radiometer Suite (VIIRS) sensor for the 2012–2022 period, applying the same CbPM model to ensure a consistent comparison (see Supplementary Fig. S10 for the full seasonal trend comparison). The results show that the winter NPP trend derived from VIIRS (0.4 TgC yr^{-1} , $P < 0.05$) is highly consistent with the trend observed from MODIS (0.3 TgC yr^{-1} , $P < 0.05$). While the absolute NPP values from VIIRS are slightly lower than those from MODIS, the remarkable consistency in the trends between these two independent

passive sensors confirms the result obtained by this type of instrument across all seasons. Crucially, both of these passive sensor trends are more than five times smaller than the trend derived from CALIOP (2.2 TgC yr^{-1} , $P < 0.05$), providing strong independent evidence that passive ocean color remote sensing significantly underestimates the recent acceleration of Antarctic winter NPP. This underscores the necessity of active LiDAR measurements for capturing these critical polar dynamics.

Distinct subregional trends and seasonal cycles

Building upon the overall analysis of polar winter NPP trends, subregional analyses were performed to investigate seasonal NPP dynamics across key sectors of the SSIZ.

The Pan-Antarctic SSIZ was divided into five key subregions including the Weddell Sea (WS), south Indian Ocean (SIO), southwestern Pacific Ocean (SPO), Ross Sea (RS), and Bellingshausen–Amundsen Sea (BAS). Specifically, the WS and RS are known for their high nutrient availability and increased light penetration as sea ice retreats, while the SIO and BAS are more constrained by lower nutrient concentrations and light availability. The SPO, with its persistent sea ice cover, presents a unique case for examining the effects of prolonged ice cover on NPP.

The NPP from 2007 to 2022 (Fig. 3a) markedly increases across most subregions, particularly in the WS and RS. The steepest annual increase of 7 TgC yr^{-1} is observed in the WS, followed by the RS with an increase of 5 TgC yr^{-1} . These robust increases align with reduced sea ice concentrations⁵⁰, which have increased light penetration and thus facilitated greater production in these regions. Moderate increases are observed in the SIO (4 TgC yr^{-1}) and BAS (2 TgC yr^{-1}). A smaller increase of 1 TgC yr^{-1} is found in the BAS, reflecting persistent environmental constraints, such as lower light availability and nutrient deficiencies, in this region. These trends highlight the significant role of changing sea ice conditions in driving primary production across the SSIZ, with notable regional differences in NPP responses.

On the basis of the more complete wintertime data obtained with CALIOP, the full seasonal cycles, referring to the entire annual cycle of primary production (Fig. 3), clearly reveal differences in the timing and magnitude of production across subregions. Monthly variations contribute to the seasonal cycle, especially production peaks, which complements these differences across subregions (Fig. S6). Notable seasonal cycles are observed in the WS (Fig. 3b) and RS (Fig. 3f), with significant summer production peaks occurring in January. The CALIOP-derived NPP data (solid lines with circles) capture these seasonal dynamics more effectively than the MODIS-derived NPP data (dashed lines with triangles), as they provide continuous measurements during the winter months, including periods of reduced sunlight.

Notably, in the BAS, RS, and SPO (Fig. 3e–g), NPP begins to increase as early as June during austral winter. The data presented in Fig. S6 reflect this early winter increase, particularly in regions where sea ice is thinning or seasonally retreating. This pattern suggests that reduced ice cover may allow more light penetration, supporting phytoplankton growth despite overall low-light conditions. Increased primary production during these winter months contributes to the uptake of carbon in the Southern Ocean, which plays a crucial role in the global carbon cycle. This finding also has important implications for understanding changes in the Southern Ocean's carbon cycle, which may affect its role in global carbon sequestration. The inability of MODIS to capture this phenomenon further underscores the need for year-round monitoring using active remote sensing methods, such as CALIOP.

The contrasting trends and seasonal cycles emphasize the spatial heterogeneity of Antarctic production. The strong increases in NPP in the WS and RS reflect the critical role of increased light penetration under thinning sea ice, whereas the limited changes in NPP in the SPO highlight the ongoing influence of increased ice concentration and prolonged ice cover as shown in Fig. S3. These results underscore the

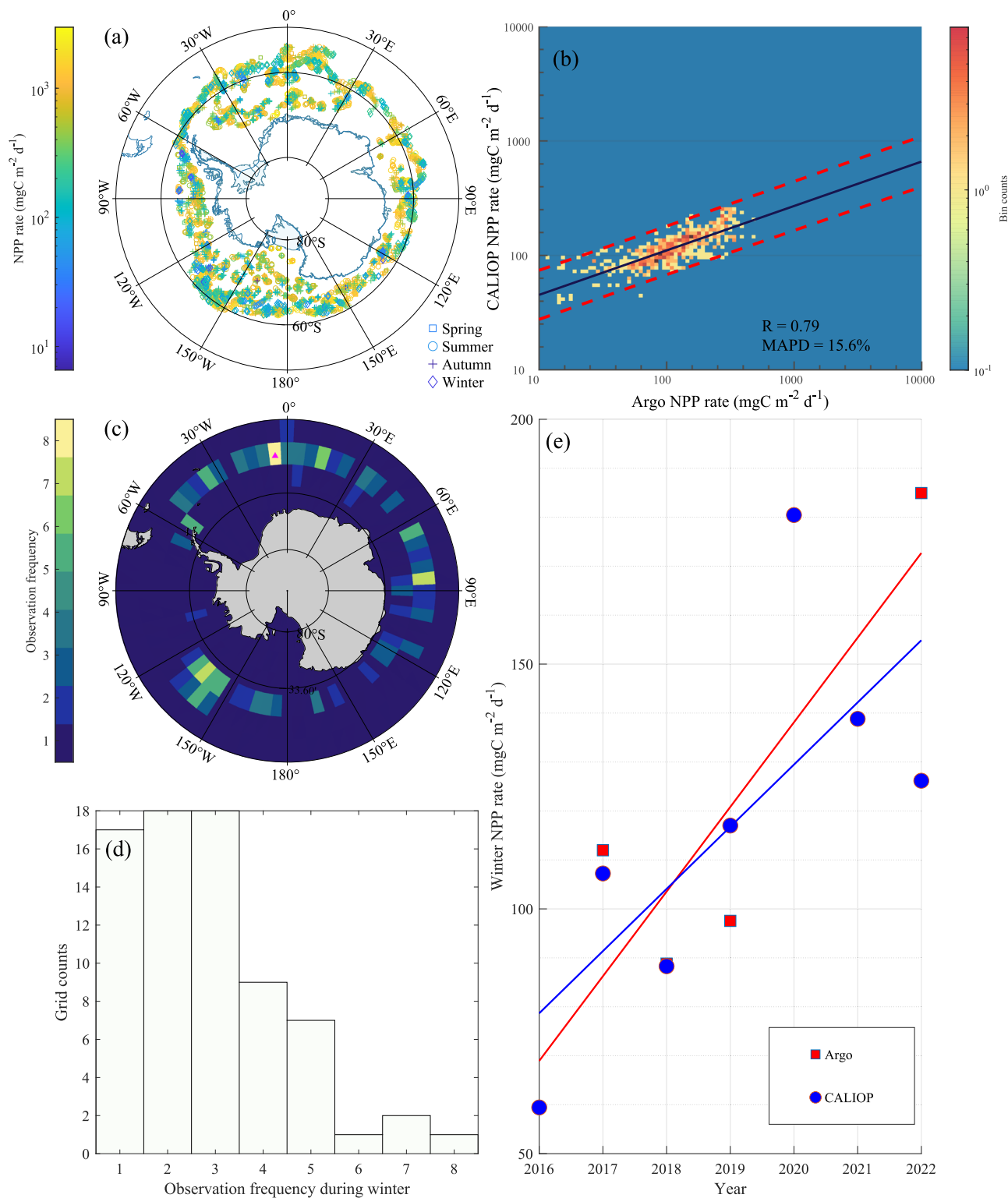


Fig. 2 | Validation of CALIOP-derived NPP with biogeochemical (BGC)-Argo data. **a** Spatial distribution of net primary production (NPP) derived from BGC-Argo data in the seasonal sea-ice zone (SSIZ) from 2012 to 2023. **b** Scatter plot comparing NPP estimates from BGC-Argo and CALIOP in winter. The black solid line represents the linear fit, and the red dashed lines indicate the 95% prediction band. **c** Spatial distribution of winter observation frequencies in a $5^{\circ} \times 4^{\circ}$ grid derived

from BGC-Argo data (2012–2023). **d** Histogram of grid counts showing winter observation frequencies, where most grids ($5^{\circ} \times 4^{\circ}$) contain fewer than five observations, underscoring data scarcity. **e** NPP trend ($\text{mgC m}^{-2} \text{d}^{-1}$) for the grid with the highest observation frequency, revealing an upward trend. **e** The red squares represent Argo data and the blue circles represent CALIOP data.

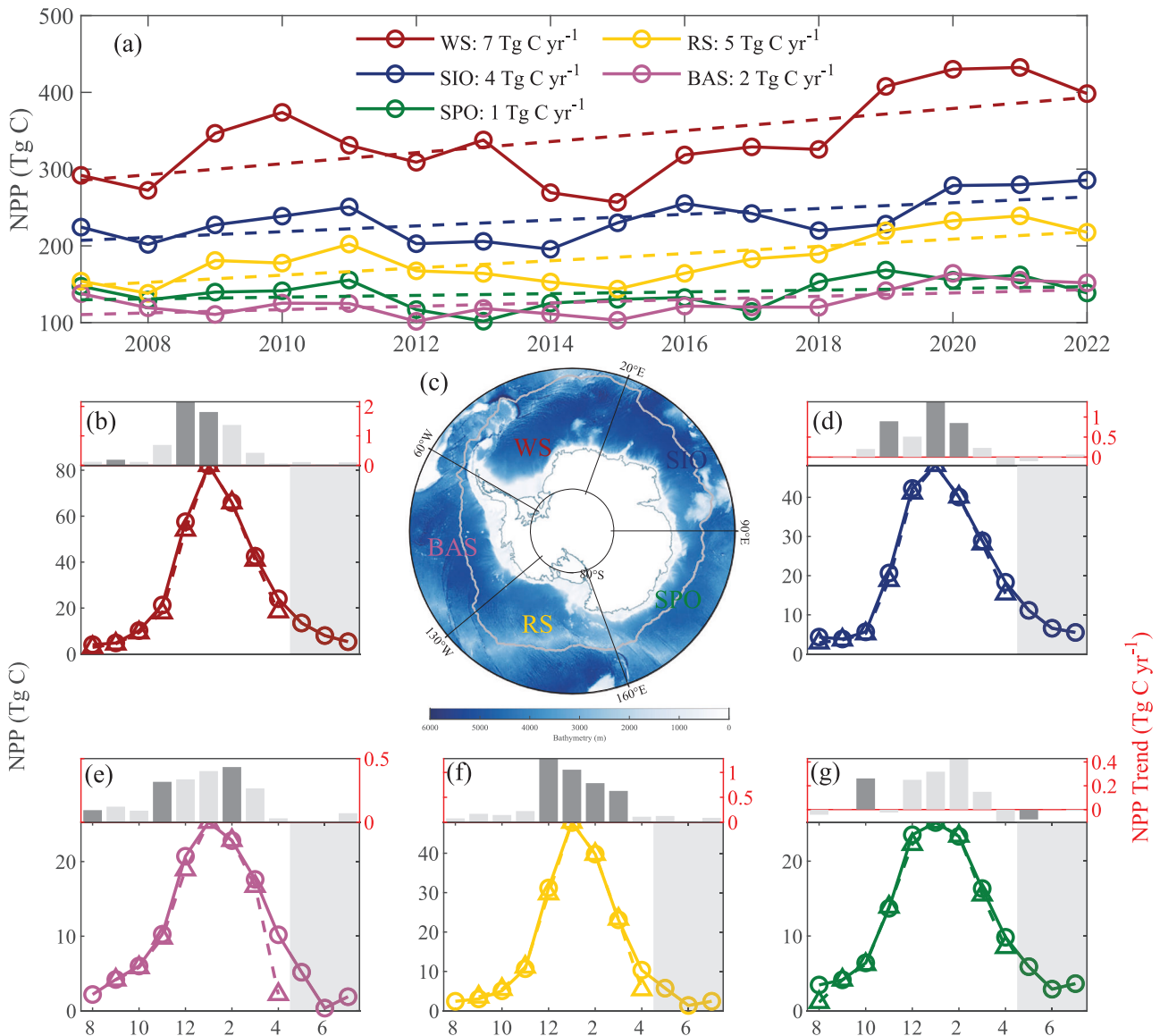


Fig. 3 | Temporal trends and full seasonal cycles of net primary production (NPP) in Antarctic subregions from 2007–2022. **a** Annual NPP trends (Tg C) from 2007 to 2022 across five subregions of the Antarctic Ocean: the Weddell Sea (WS), South Indian Ocean (SIO), Southwestern Pacific Ocean (SPO), Ross Sea (RS), and Bellingshausen–Amundsen (BAS). The solid lines represent NPP estimates derived from CALIOP, and the dashed lines indicated linear trends. The slopes of the trends are annotated in the legend. **b** Seasonal NPP variations in the Weddell Sea (WS). **c** Subregion boundaries displayed on a polar stereographic map. The gray line

represents the seasonal sea ice zone (SSIZ). Seasonal NPP variations in **(d)** the South Indian Ocean (SIO), **(e)** the Bellingshausen–Amundsen Sea (BAS), **(f)** the Ross Sea (RS), and **(g)** the Southwestern Pacific Ocean (SPO), highlighting the differences between CALIOP (solid lines with circles) and MODIS (dashed lines with triangles). The gray shading indicates the periods that are unavailable from the MODIS observations due to the unavailability of sunlight. The dark and light gray bars in the top portions of the graphs indicate that the trends in the corresponding months are statistically significant and insignificant at the 95% confidence level, respectively.

importance of active remote sensing techniques, such as CALIOP, in capturing production trends during the polar night that are otherwise underestimated by passive remote sensing instruments, such as MODIS.

Shifts in seasonal driver of Antarctic subregional NPP

To better understand the environmental drivers of NPP across Antarctic subregions, we examined key oceanographic parameters that influence primary production. Generally, sea surface temperature (SST) plays a key role in regulating metabolic rates, which refers to the rate at which organisms like phytoplankton grow and respire, and stratification, which is the layering of water masses in the ocean that affects the mixing of nutrients between surface and deeper waters. These factors influence the timing and magnitude of phytoplankton production peaks^{51–53}. Sea surface salinity (SSS) is another important

factor that influences production by affecting water column stability and nutrient mixing⁵⁴. Low SSS can cause stronger stratification, limiting vertical mixing and nutrient transport to the surface, which reduces production. Moreover, sea surface wind (SSW)-induced mixing is a critical physical process that enhances vertical nutrient transport, particularly in regions where upwelling occurs, and this process contributes to the availability of nutrients essential for phytoplankton growth⁵⁵. A greater mixed layer depth (MLD) enhances the supply of nutrients from deeper waters to the surface, playing a vital role in sustaining production in the Southern Ocean⁵⁶. Furthermore, sea ice dynamics indicated by sea ice concentration (SIC), which refers to the fraction of the ocean surface covered by sea ice, influence light availability and nutrient mixing^{57,58}. The extent of sea ice significantly affects the timing of phytoplankton blooms, as thinner ice allows more light to penetrate, thus increasing production⁵³. In addition, key

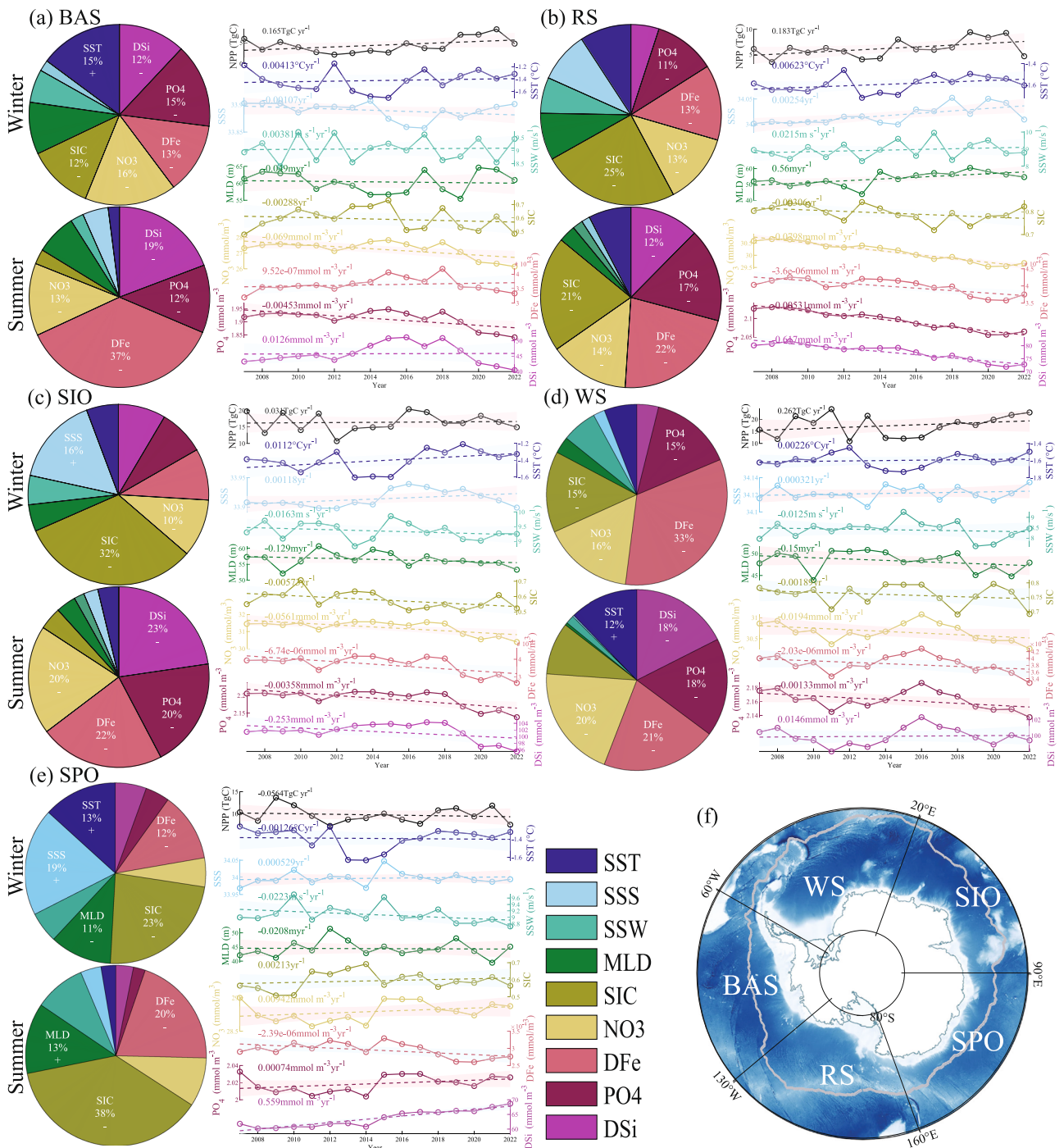


Fig. 4 | Drivers of seasonal and regional net primary production (NPP) variation. Contribution ratios of environmental parameters (sea surface temperature (SST), sea surface salinity (SSS), sea surface wind (SSW), mixed layer depth (MLD), sea ice concentration (SIC), nitrate (NO₃), dissolved iron (DFe), phosphate (PO₄), and dissolved silica (DSi)) to NPP variation in the **a** Bellingshausen-Amundsen (BAS), **b** Ross Sea (RS), **c** South Indian Ocean (SIO), **d** Weddell Sea (WS), and **e** Southwestern Pacific Ocean (SPO) during austral wintertime (upper-left pie chart in each panel) and summertime (lower-left pie chart in each panel) and trends in NPP and environmental parameters (right half of each panel) during austral wintertime in the Antarctic subregions. Note: the plus or minus signs on the pie charts indicate positive or negative correlations, respectively. **f** Map displaying the boundaries of the five subregions analyzed: Weddell Sea (WS), South Indian Ocean (SIO), Southwestern Pacific Ocean (SPO), Ross Sea (RS), and Bellingshausen-Amundsen (BAS).

(lower-left pie chart in each panel) and trends in NPP and environmental parameters (right half of each panel) during austral wintertime in the Antarctic subregions. Note: the plus or minus signs on the pie charts indicate positive or negative correlations, respectively. **f** Map displaying the boundaries of the five subregions analyzed: Weddell Sea (WS), South Indian Ocean (SIO), Southwestern Pacific Ocean (SPO), Ross Sea (RS), and Bellingshausen-Amundsen (BAS).

nutrients, including nitrate (NO₃), phosphate (PO₄), dissolved silica (DSi), and dissolved iron (DFe), are essential for phytoplankton growth, and their availability drives production in the Southern Ocean⁵⁹.

Here we use random forest (RF) models to capture the contributions of these environmental parameters and nutrients to the NPP in the above-outlined Antarctic subregions. Through this model, the

seasonal variations in the contributions of the abovementioned environmental parameters to NPP across Antarctic subregions were investigated. We first investigated the contributions of these parameters during austral winter, a period that was previously unexplored due to the lack of winter NPP data in the Antarctic region. In the BAS (Fig. 4a), the key contributors to NPP are NO₃ (16%), SST (15%), and PO₄ (15%), reflecting the critical role of nutrients and temperature in

supporting limited production under thick ice cover, which supports the moderate increase in NPP (2 Tg C yr^{-1}) in the BAS. On the other hand, in the RS (Fig. 4b), SIC (25%) is the dominant driver, along with NO_3 (13%) and DFe (13%), suggesting that the significant increase in NPP (5 Tg C yr^{-1}) in the RS is driven by reduced SIC, which enhances light penetration and improves light conditions. Similarly, in the SIO (Fig. 4c), SIC (32%) and SSS (16%) are the primary contributors, with NO_3 (10%) also playing a notable role. This underscores that the moderate increase in NPP (4 Tg C yr^{-1}) in the SIO is driven by SIC and SSS, which influence water column stability and nutrient availability. In the WS (Fig. 4d), DFe (33%), NO_3 (16%), and PO_4 (15%) are the dominant drivers, suggesting that despite the limited light in this region, the supply of essential nutrients is critical for sustaining low but persistent phytoplankton growth in this iron-limited region⁶⁰. However, a different pattern is observed in the SPO (Fig. 4e), where the SIC (23%), SST (13%), SSS (19%) and MLD (11%) are the leading contributors. This highlights the roles of physical mixing and heat flux in driving productivity during the polar night. SIC and SSS influence the stratification and stability of the water column, while SST and MLD are indicators of the thermal and mixing conditions that affect nutrient availability and light penetration. These factors, together, drive the production despite the low light conditions in winter, which influence the weaker increase in NPP (1 Tg C yr^{-1}) in the SPO. Thus, during the austral winter, physical factors are dominant because of limited sunlight and extensive sea ice cover.

We next investigated the trends in these parameters during austral summer. In the BAS (Fig. 4a), DFe (37%), DSi (19%), and NO_3 (13%) dominate, underscoring the importance of nutrient synergy (i.e., the combined availability of multiple nutrients) in supporting high production during this period. Similarly, in the RS (Fig. 4b), DFe (22%), NO_3 (14%), and SIC (21%) are the major drivers, reflecting the combined influence of nutrient availability and sea ice-driven nutrient resupply. DFe and NO_3 directly contribute to phytoplankton growth by providing essential nutrients, whereas SIC plays a role in the seasonal resupply of nutrients by influencing the movement and melting of sea ice, which brings nutrients from deeper layers of the ocean to the surface, enhancing nutrient availability during critical periods of primary production. In the SIO (Fig. 4c), the leading contributors are DSi (23%), DFe (22%), NO_3 (20%), and PO_4 (20%), emphasizing the central role of nutrient and trace metal availability. The availability of these key nutrients, particularly DSi, DFe, and NO_3 , supports phytoplankton growth by providing essential resources for cellular processes. The WS (Fig. 4d) shows a relatively balanced contribution from DFe (21%), NO_3 (20%), and PO_4 (18%), with DFe being the dominant driver. This suggests that while iron plays a significant role, the similar contributions of nitrate and phosphate indicate that multiple nutrients are limiting primary productivity in the region. In the SPO (Fig. 4e), SIC (38%), DFe (20%), and MLD (13%) emerge as the key drivers, with sea ice coverage and vertical mixing playing critical roles in enhancing nutrient availability during this period of elevated production. Thus, during austral summer, nutrient availability is the predominant controller of NPP across all regions, reflecting heightened biological demand for nutrients during the peak growing season. These nutrients provide the essential resources for phytoplankton growth, and their availability directly influences NPP. The combined effect of DFe, nitrate, and phosphate determines the overall nutrient supply, which is critical for sustaining primary production during the peak growing season.

A clear seasonal contrast emerges from this analysis. In particular, the results of the RF model underscore the distinct differences in the importance of these drivers (environmental parameters) between austral winter and summer, reflecting the interplay of light, nutrient availability, and sea ice dynamics. During winter, physical parameters such as the SIC, SSS, SST, and MLD dominate by regulating light availability and stratification under harsh conditions. When water temperature rises, the rate of photosynthesis may increase, which

could enhance the overall NPP in these areas⁶¹. Additionally, ice melt or extended melting periods lead to increased daylight hours, directly stimulating phytoplankton growth⁶². In summer, the biological demand for nutrients such as DFe and NO_3 , becomes the primary control, reflecting a seasonal shift from physical to biological regulation of production. This seasonal shift can lead to a negative correlation between NPP and nutrient concentrations. As NPP increases rapidly during summer blooms, phytoplankton efficiently utilize available nutrients, potentially leading to a drawdown in dissolved nutrient concentrations¹³. The temporal trends in NPP and the environmental drivers reveal remarkable increases in production between 2007 and 2022 in regions such as the RS and WS, and these increases are closely linked to reductions in SIC during winter (Fig. S3). As SIC decreases, more sunlight penetrates the water, enhancing light availability for phytoplankton growth. In contrast, more stable NPP is observed in the BAS, suggesting persistent environmental constraints such as increasing sea ice concentration (Fig. S3) despite seasonal shifts in the importance of drivers.

Mechanistic explanations of Antarctic NPP variation

Understanding the mechanisms underlying Antarctic NPP variation is critical for exploring how environmental and climatic factors drive primary production in the Southern Ocean. With the above results in seasonal data analysis, including the incorporation of winter data, a more complete examination of NPP variations over a full seasonal cycle is now possible. By employing the partial correlation and multiple conditional independence (PCMCI+) algorithm, in this study, the causal relationships between Antarctic NPP and key climatic and environmental factors, such as SIC, SST, DFe, and the southern annual mode (SAM), are quantitatively assessed. The SAM describes the pressure difference between the middle and high latitudes of the Southern Hemisphere and is closely related to Antarctic climate dynamics⁶³. PCMCI+ algorithm was chosen due to its ability to effectively capture complex, non-linear causal relationships and interactions between multiple variables^{64,65}. This approach provides a deeper understanding of how local environmental conditions and remote climate systems, including phenomena such as the SAM, El Niño-Southern Oscillation (ENSO), and the Indian Ocean Dipole (IOD) interact with Antarctic ecosystems, highlighting the potential impacts of climate change on NPP dynamics. The PCMCI+ analysis reveals how the temporal lags and feedback mechanisms between environmental factors shape subregional variations in NPP and its seasonal cycles. As illustrated in Fig. 5, the causal network, which represents the relationships between different environmental and climatic factors and NPP, visually shows interactions between NPP and various drivers, including climate indices, environmental factors, and nutrients indices. The blue and red lines indicate positive and negative causal influences, respectively, with the PCMCI+ algorithm quantifying the strength of these causal relationships. This network underscores the complexity of Antarctic NPP variability, which is shaped directly by local conditions, remote climate events, and their temporal lags and feedbacks across seasons.

The SAM has emerged as the dominant mode of atmospheric variability influencing Antarctic climate and ecological systems⁶⁶. Acting over monthly to decadal timescales, the SAM modulates atmospheric circulation, shaping sea ice distributions, temperature gradients, and wind patterns in the Southern Ocean⁶⁷. Analysis with the PCMCI+ algorithm highlights the pivotal role of the SAM, revealing strong causal links between the SAM and NPP variability across subregions (Fig. 5). Persistent positive SAM phases⁶⁷, characterized by poleward shifts in westerly winds, typically reduce the extent of sea ice, increase light penetration and promote phytoplankton growth^{68,69}. These effects are particularly pronounced in regions such as the WS (Fig. 5b) and RS (Fig. 5e), where NPP peaks often coincide with the timing of ice retreat. In general, the positive phase of SAM induces

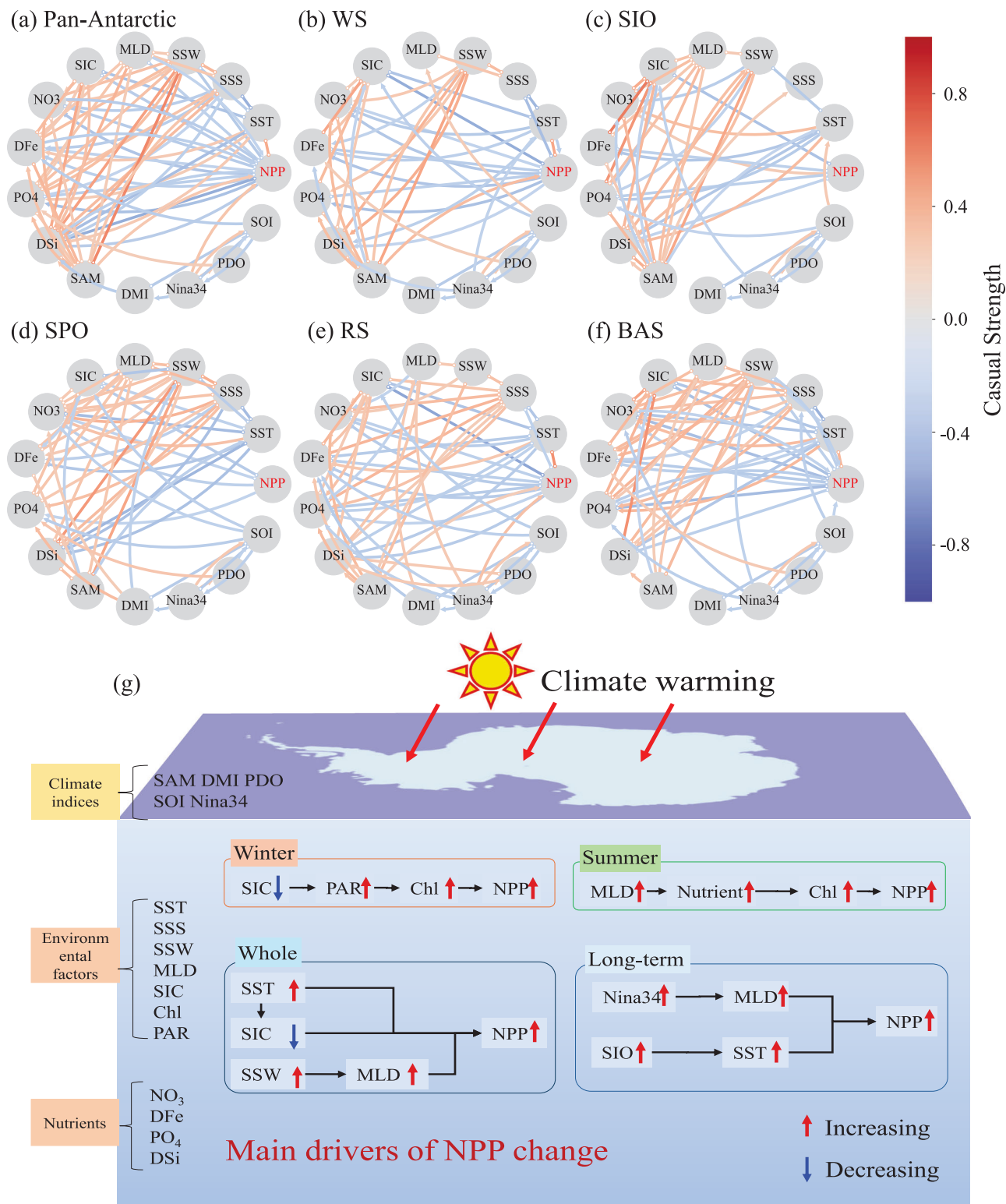


Fig. 5 | Causal relationships between Antarctic net primary production (NPP) and climatic/environmental factors and schematic diagram of the mechanisms of Antarctic NPP trends. **a** All pan Antarctic regions combined and **b** Weddell Sea (WS), **c** South Indian Ocean (SIO), **d** Southwestern Pacific Ocean (SPO), **e** Ross Sea (RS), and **f** Bellingshausen-Amundsen (BAS) individual subregions. In panels

a-f the blue lines/arrows indicate positive causal influences, whereas red lines/arrows represent negative influences. The specific time lags (in months) for each causal relationship are detailed in Table S1. **g** Schematic diagram of the mechanisms of Antarctic NPP trends in response to climate change.

stronger westerly winds, which promotes the upwelling of warmer subsurface waters, increases the salinity of surface waters, and weakens stratification. This process triggers deep convection, bringing more subsurface warm, saline water to the surface, which leads to a

reduction in sea ice⁷⁰. This phenomenon aligns with the sharp increase in NPP after 2014. Moreover, the SAM plays a critical role in driving changes in the MLD and mesoscale eddy activity^{71,72}, which in turn affect nutrient distributions and fluctuations in phytoplankton²⁰.

In addition to the SAM, other climatic factors, such as El Niño–Southern Oscillation (ENSO), significantly influence the Antarctic marine environment through teleconnections, which refer to the long-distance connections between climate phenomena in different regions, and lagged effects⁷³, which describe the delayed response of one variable to changes in another. The PCMC1+ algorithm results reveal that tropical climate phenomena, such as the southern oscillation index (SOI) and ENSO, impact NPP indirectly through changes in atmospheric and oceanic circulation (Fig. 5). ENSO events can alter Southern Hemisphere wind patterns, affecting sea ice dynamics⁷³ in Antarctic waters. ENSO generally influences the Antarctic climate and sea ice distribution in two ways: (1) ENSO events, especially El Niño, enhance convective activity in the tropical Pacific, triggering Rossby waves in the atmosphere. These waves propagate toward the poles and ultimately affect atmospheric circulation in the Antarctic region; (2) ENSO events also excite the Pacific–South America (PSA) teleconnection pattern, an anomalous atmospheric circulation mode that causes pressure anomalies in the South Pacific and Antarctic regions^{74,75}. These lagged relationships, revealed by PCMC1+, suggest that tropical climate anomalies can influence Antarctic production several months later.

As global climate warming progresses, its influence on the Antarctic ecosystem is becoming increasingly evident. The ongoing reduction in sea ice extent, as seen in recent decades, has amplified the role of winter NPP in contributing to overall carbon sequestration. Fig. 5g illustrates the mechanisms underlying the trends in Antarctic NPP in response to climate change. During the winter months, reductions in SIC lead to increased photosynthetically active radiation (PAR) that refers to the portion of sunlight that plants use for photosynthesis, which in turn enhances *Chla* and subsequently increases NPP. In summer, a greater MLD provides greater access to nutrients, fostering *Chla* growth and increasing NPP^{76,77}. Over long-term scales, which in this study refers to periods greater than six months, changes such as increases in Niño 3.4 and SST in the SIO further increase NPP (Fig. 5c). These findings collectively highlight the complex interplay between local environmental conditions and remote climate systems in regulating Antarctic NPP, providing a crucial foundation for understanding future changes in primary productivity under ongoing climate change.

Ecological implications

The observed considerable increase in Antarctic winter NPP fundamentally alters our understanding of the role of the Southern Ocean in global carbon cycling and ecosystem dynamics. Traditionally, Antarctic winter has been considered a period of biological dormancy due to extreme light limitations and extensive sea ice cover²⁹. However, emerging evidence highlights winter NPP as a critical contributor to carbon sequestration, ocean–atmosphere interactions, and biogeochemical processes, thereby redefining the Southern Ocean’s role as a year-round carbon sink⁷⁸. This finding aligns with recent studies, which demonstrate that photosynthesis can occur at extreme low light levels²⁸. Enhanced winter NPP drives substantial production of particulate organic carbon (POC), which is exported below the euphotic zone via a biological pump, enabling long-term storage of atmospheric CO₂ in the deep ocean⁷⁹. This process bolsters the Southern Ocean’s efficiency in offsetting anthropogenic CO₂ emissions, transforming it into a more effective buffer against global climate change⁸⁰. The concomitant reduction in the surface water partial pressure of CO₂ (pCO₂) strengthens the air–sea CO₂ gradient, especially in ice–edge regions where diminishing sea ice promotes greater gas exchange⁸¹. These findings underscore the previously underappreciated importance of winter processes in shaping global carbon fluxes, highlighting the crucial role of Antarctic winter NPP in carbon sequestration and its potential implications for future climate modeling and ecosystem dynamics.

The ecological ramifications of increased winter NPP observed in this study extend beyond carbon cycling, with the potential to reshape the phytoplankton community structure and ecosystem impacts on higher trophic levels. A sustained increase in winter biomass has the potential to reshape the phytoplankton community structure that overwinters and initiates the subsequent spring bloom. A shift in the dominant cell size or species could alter trophic transfer efficiency and hence higher trophic production and the community composition of zooplankton and other predators^{82,83}. Increased winter production may favor diatom propagation. While these cells contribute disproportionately to POC export and biological pump efficiency^{84,85}, they are also a critical, high-quality food source for grazers like Antarctic krill. Therefore, any change in the abundance or timing of these diatom populations could have cascading impacts on the food web, affecting the krill that are a vital link to higher trophic levels such as penguins, seals, and whales⁸⁶. These changes in primary production could enhance the ocean’s ability to sequester carbon by promoting the export of particulate organic carbon to deeper waters. Conversely, if increased winter NPP leads to greater activity of coccolithophores, which are producers of particulate inorganic carbon (PIC), this could reduce the oceanic sink for atmospheric CO₂ in the short-term by increasing near-surface pCO₂, with cascading effects on nutrient cycling and ecosystem functioning^{87–90}. The role of sea ice dynamics is pivotal: reduced ice cover increases light penetration⁹¹ and nutrient availability, whereas episodic mixing events resupply macronutrients and trace metals, such as nitrate and dissolved iron, respectively, to surface waters^{92,93}. Our results indicate that the interplay among physical and biological processes sustains winter production even under low-light conditions, challenging long-held assumptions about polar ecosystem dormancy during the austral winter. These dynamics also amplify ocean–atmosphere feedbacks, modifying local heat fluxes, wind-driven mixing, and nutrient transport, with far-reaching consequences for regional climate regulation and energy balance¹⁹.

Our results show that Antarctic winter NPP has rapidly increased over the past decade, with an annual growth rate of 2.24 Tg C/year in the past decade, making it a significant component of the Southern Ocean’s carbon storage. Given this increasing trend, it is essential to include winter NPP in global carbon models, as its contributions have historically been underestimated or omitted. While global ocean NPP trends show overall decreases^{35,36}, Antarctic winter NPP shows a particularly strong increasing trend, highlighting its increasing role in the Southern Ocean’s carbon dynamics. Its potential impact on POC export and surface pCO₂ dynamics positions it as a critical driver of global carbon fluxes, necessitating its integration into biogeochemical and Earth system models. These shifts are particularly relevant given the Southern Ocean’s disproportionate contribution to global carbon uptake^{1–3} and its sensitivity to anthropogenic climate forcing. The continued increase in Antarctic winter NPP is a key trend that could offset or mitigate declines in NPP observed in other oceanic regions³⁵. Furthermore, this growing recognition of Antarctic winter NPP underscores a revelation of previously unrecognized potential for carbon fixation, suggesting that this previously overlooked component could significantly influence global carbon dynamics²⁸.

The drivers of this unexpected increase in winter production reflect the interplay of regional and global climatic factors. The SAM is shown as a primary regulator, influencing the SIC, mixed layer dynamics, and light availability. The positive phases of the SAM, characterized by poleward-shifted westerlies, reduce SIC and increased light penetration, creating favorable conditions for enhanced NPP in high-latitude regions^{68,69,71,72}. Our results provide evidence that these processes are driving significant NPP increases specifically in the WS and RS, highlighting the regional variability in the response of primary production to SAM fluctuations. Concurrently, teleconnections with tropical climate phenomena, such as ENSO, introduce additional complexity. For example, ENSO-induced

atmospheric anomalies influence zonal sea ice drift, nutrient resupply and stratification in the Southern Ocean^{94,95}, with lagged effects on production⁹⁶. These findings emphasize the interconnectedness of global climate systems and the need for a holistic understanding of how remote drivers interact with local processes to shape Antarctic ecosystems.

As the Antarctic ecosystem has undergone rapid transformation due to climate warming and sea ice loss⁹⁷, understanding the mechanisms underlying winter NPP is essential for predicting future changes in the global carbon cycle. The interplay of increased light availability, nutrient dynamics, and community shifts highlights the dynamic and evolving nature of Antarctic production⁹⁸. By utilizing CALIOP for obtaining NPP data in winter and integrating full seasonal cycle analyses into existing frameworks, this study provides a paradigm for understanding Southern Ocean ecosystems under changing climatic conditions. Future research should prioritize extreme climatic events, such as marine heatwaves and anomalous wind patterns, which could exacerbate or mitigate the observed trends. This knowledge is critical not only for refining predictions of Antarctic ecosystem resilience but also for assessing the Southern Ocean's role in regulating the global climate and supporting biodiversity in an era of unprecedented environmental change.

Methods

Data acquisition

Multiple data sources, including MODIS, CALIOP, and BGC-Argo datasets, are used to investigate Antarctic NPP dynamics. The MODIS-Aqua Level 3 9-km daily products including b_{bp} , $Chla$, and K_d available at <https://oceancolor.gsfc.nasa.gov/>, serve as key predictors. MODIS data were strategically chosen to train our TBTS model because both MODIS (on the Aqua satellite) and CALIOP (on the CALIPSO satellite) are part of the A-Train constellation, with observation times separated by only ~90 seconds. This near-simultaneous data acquisition is crucial for machine learning as it minimizes the temporal mismatch between the LiDAR signal and the ocean color properties, thereby reducing a significant source of uncertainty in model training. CALIOP Level-1B V4.1⁹⁹ and Level-2 Merged Layer V4.20 products are used to acquire LiDAR-derived oceanographic parameters from 16,236 tracks spanning from 2006 to 2023. These data include backscatter measurements and attenuated backscatter data, which are crucial for understanding phytoplankton dynamics. These LiDAR parameters are used to calculate K_d , $Chla$, and b_{bp} , which are related to the distributions of photosynthetically active radiation and phytoplankton carbon³⁴. Then they are integrated into the NPP model. The biogeochemical Argo (BGC-Argo) dataset^{100–102}, which provides in situ measurements, is used for model validation. This dataset includes direct measurements of $Chla$ and other biogeochemical parameters accessible via the Argo Global Data Assembly Center (GDACs) at Ifremer (<ftp://ftp.ifremer.fr/ifremer/argo/>).

The data sources for the evaluated parameters are as follows. The Global Ocean OSTIA Sea Surface Temperature and Sea Ice Reprocessed product (SST-GLO-SST-L4-REP-OBSERVATIONS-010-011)¹⁰³ provides SST Level-4 data. The Multi Observation Global Ocean Sea Surface Salinity and Sea Surface Density product (MULTIOBS_GLO_PHY_S_SURFACE_MYNRT_015_013)^{104–106} provides SSS Level-4 data. The Global Ocean Monthly Mean Sea Surface Wind and Stress from Scatterometer and Model product (WIND_GLO_PHY_CLIMATE_L4_MY_012_003) provides SSW Level-4 data. The Multi Observation Global Ocean 3D Temperature Salinity Height Geostrophic Current and MLD product (MULTIOBS_GLO_PHY_TSUV_3D_MYNRT_015_012)^{107,108} provides MLD Level-4 data. Data on sea ice extent and concentration are accessed from the Sea Ice Index extent data obtained from the National Snow and Ice Data Center (NSIDC)¹⁰⁹. The Global Ocean Biogeochemistry Hindcast product from the Copernicus Marine

Environment Monitoring Service (CMEMS) provides Level-4 data for key nutrients, including nitrate (NO_3), phosphate (PO_4), dissolved silica (DSi), and iron (DFe) (GLOBAL_MULTIYEAR_BGC_001_029). Data on the SAM are available from Marshall's SAM Index page (<https://legacy.bas.ac.uk/met/gjma/sam.html>). Data on other climate indices in anomaly format for the period of 1978–2022 are available from the Global Climate Observing System website (<https://psl.noaa.gov/data/timeseries/month/>). These indices include Niño 3.4, which tracks SST anomalies in the equatorial Pacific region (5°S to 5°N, 170°W to 120°W)¹¹⁰; the SOI, which represents the normalized pressure difference between Tahiti and Darwin¹¹¹; the Pacific Decadal Oscillation (PDO), which describes a long-term El Niño-like climate variability pattern in the Pacific at 20°N¹¹²; and the dipole mode index (DMI), which is defined by the anomalous SST gradient between the western equatorial Indian Ocean (50°E to 70°E, 10°S to 10°N) and the southeastern equatorial Indian Ocean (90°E to 110°E, 10°S to 0°N)¹¹³.

CALIOP data preprocessing

For CALIOP data, the 532 nm echo signal is split into vertical and parallel components using a polarization beam splitter (PBS), and these components are detected by photomultiplier tubes (PMTs)¹¹⁴. However, the transient response of the detector causes the recorded signal intensity to exceed the actual backscatter intensity after strong signals from sources such as the Earth's surface or dense clouds are detected. Initially, the signal decreases as expected, but it eventually decays at a slower rate resembling an exponential function¹¹⁵. To correct for this, a deconvolution process is applied to the measured signals¹¹⁶:

$$\beta'(z) = [F]^{-1}\beta(z). \quad (1)$$

where $\beta'(z)$ is the corrected backscatter signal, $\beta(z)$ is the measured signal, and $[F]$ is the matrix form of the transient function.

Owing to the imperfect PBS, part of the parallel polarization component leaks into the vertical polarization component, which is a phenomenon known as polarization crosstalk. To eliminate this effect, the following corrections are made¹¹⁷:

$$\beta_{\parallel,c} = \frac{\beta_{\parallel,m}}{1 - CT} \quad (2)$$

$$\beta_{\perp,c} = \beta_{\perp,m} - CT \times \beta_{\parallel,c} \quad (3)$$

where $\beta_{\parallel,c}$ and $\beta_{\perp,c}$ are the corrected parallel and vertical signals, respectively. $\beta_{\parallel,m}$ and $\beta_{\perp,m}$ are the parallel and vertical signals corrected for the transient response. CT represents the crosstalk.

Next, the total column-integrated depolarization ratio δ_T which includes both surface backscatter and subsurface backscatter, is computed as follows:

$$\delta_T = \frac{\sum_{i=p}^{i=p+2} \beta_{\perp,c}}{\sum_{i=p}^{i=p+2} \beta_{\parallel,c}} \quad (4)$$

where p represents the range bin of the peak surface return¹¹⁸.

Finally, to calibrate the ocean surface backscatter, the subsurface cross-polarized component of the column-integrated backscatter β_W is calculated as follows⁴⁴:

$$\beta_W = \delta_T \frac{\beta_S}{1 - 10\delta_T} \quad (5)$$

where β_S denotes the LiDAR surface backscatter, which is estimated using collocated sea surface wind speed data¹¹⁹.

To eliminate the impact of sea ice on CALIOP observations in polar regions, we selectively included data where δ_T less than 0.05, effectively excluding areas with full or partial sea ice coverage, given that sea ice tends to have a high depolarization ratio⁴⁴. We further ensured data integrity by retaining only those measurements with integrated attenuated backscatter values less than 0.017 sr^{-1} , which indicates clear atmospheric conditions¹¹⁸. Additionally, to reduce interference from ocean surface phenomena such as foam and white caps, which are prevalent at high wind speeds, and to prevent signal saturation at low wind speeds, we included only data captured at wind speeds between 2 m/s and 9 m/s^{44,116}.

Antarctic phytoplankton NPP derived from CALIOP

A two-branch-two-step (TBTS) model is used to derive $Chla$, b_{bp} , K_d from the CALIOP data (Fig. S7). The deep learning model developed in this study consists of two branches: a waveform branch and a physical parameter branch. This structure leverages both deep learning techniques and physical parameter inputs¹²⁰. Unlike traditional deep learning methods that rely solely on waveform data, this model incorporates data on additional physical parameters, i.e., δ_T and β_W , allowing for more seamless and effective integration of physical and observational data. By incorporating physical parameters as a second branch, the model can better account for the underlying physical processes, thereby improving its performance in oceanic LiDAR applications⁴⁰.

The waveform deep learning branch takes as input the corrected parallel and vertical backscatter signals within a range of 5 bins above and below the sea surface⁴⁰. Specifically, the input includes 22 variables derived from the CALIOP measurements. In the model, a convolutional neural network (CNN)¹²¹ is used to automatically extract features from these corrected signals. After processing through the CNN layers, the data are flattened into 128 features via fully connected (FC) layers. The second branch of the model addresses physical parameters, which form an integral part of the input for the network. The physical parameters include δ_T and β_W . These physical parameters are processed through FC layers for feature extraction. The features from both branches are then combined through a concatenation layer and passed through another FC layer before performing regression. The model uses Rectified Linear Units (ReLU) activation functions throughout, except for the final layer with linear activation functions to retrieve the values of b_{bp} , $Chla$, and K_d . The model is trained using the RMSprop optimization algorithm, which divides the gradient by the average of its recent magnitudes¹²².

To increase the accuracy of the model, a two-step approach is applied to reconstruct b_{bp} , $Chla$, and K_d based on the MODIS data. The first step involves the reconstruction of climatologies, which refer to the monthly climatological mean values averaged over the period 2006–2023. The second step focuses on reconstructing anomalies relative to the climatologies. This two-step approach is particularly advantageous because it mitigates issues related to sparse observational coverage and accounts for seasonal variations driven by climate change¹²³. The two steps are as follows.

Step 1: Reconstruction of climatologies: In this step, the two-branch model reconstructs the normalized monthly climatologies for b_{bp} , $Chla$, and K_d as a nonlinear function of the normalized CALIOP waveform data (β_n), $\delta_{T,n}$, and $\beta_{W,n}$:

$$(b_{bp,n}, Chla_n, K_{d,n}) = \text{TBN}(\beta_n, \delta_{T,n}, \beta_{W,n}) \quad (6)$$

Step 2: Reconstruction of anomalies: In the second step, the model reconstructs anomalies in b_{bp} , $Chla$, and K_d as a nonlinear function of the normalized waveform data and their respective anomalies:

$$(b_{bp,anom}, Chla_{anom}, K_{d,anom}) = \text{TBN}(\beta, \delta_T, \beta_W, \beta_{anom}, \delta_{T,anom}, \beta_{W,anom}) \quad (7)$$

The anomalies are calculated as the difference between collocated MODIS b_{bp} , $Chla$, and K_d measurements and the climatologies reconstructed in Step 1.

To increase model accuracy, all datasets are normalized to zero mean and a unit standard deviation before training. This normalization ensures that the ranges of all the predictors are comparable and prevents predictors with greater variability from dominating the model¹²⁴. During the training, MODIS b_{bp} , $Chla$, and K_d data and CALIOP measurements from 2006 to 2023 are used. The data are averaged along 9 km segments to align with the MODIS observations. The training dataset includes approximately 10^6 match points per month, with 10^5 points in high-latitude regions, ensuring robust model performance in polar areas. The data are randomly split, with 70% used for training, 15% for validation, and 15% for evaluation. This division ensures that the data for evaluation remain separate from the training process, thereby providing an unbiased assessment of the model's performance.

The accuracy of the model is then validated by comparing its results with in-situ BGC-Argo data from 2006 to 2023. The data are matched within a 25 km² area and 24-hour window studies^{125,126}. This ensures proper temporal and spatial alignment, providing a robust evaluation of the model's performance. As shown in Fig. S8, the model demonstrates strong performance in predicting oceanographic parameters, as evidenced by the high correlation coefficients (R values) and low root mean square deviations (RMSDs) across all the validation comparisons. For the CALIOP and MODIS data, the model achieves R values ranging from 0.85 to 0.95, indicating a robust linear relationship between the satellite-derived and observed values. The low RMSD values further highlight the model's accuracy, with only minimal deviation from the true measurements. Additionally, the mean absolute percentage deviation (MAPD) is relatively low, underscoring the model's precision and reliability in predicting b_{bp} , $Chla$, and K_d . Overall, the model's strong predictive capabilities, as demonstrated through the validation results, suggest its potential for accurate oceanographic monitoring and analysis.

After validation, the trained model is used to reconstruct b_{bp} , $Chla$, and K_d from 2006 to 2023, specifically focusing on polar regions, where traditional passive sensors like MODIS often fail to provide data. The carbon-based productivity model (CbPM)^{127,128}, a method that estimates net primary productivity from phytoplankton carbon biomass and growth rates, is subsequently used to derive net primary productivity (NPP rate) in polar regions. Notably, the CbPM accounts for photoacclimation by calculating a dynamic chlorophyll-to-carbon ratio that varies with light and temperature, a critical feature for accurately assessing productivity in variable polar environments. The NPP rate is derived based on CALIOP-derived parameters:

$$\text{NPP rate} (\text{mgC m}^{-2} \text{ d}^{-1}) = \text{carbon} \times \text{growth rate} \times \text{volume function} \quad (8)$$

where *carbon* is the phytoplankton carbon biomass that is estimated from b_{bp} ¹²⁸, *growth rate* is derived from chlorophyll-to-carbon¹²⁸, and *volume function* is expressed as a function of depth-dependent photoacclimation and vertical variations in nutrient limitations¹²⁷. To calculate the net primary production (NPP) for a specific region and period (such as for one winter or year), we accumulate NPP * cell area * number of days, at which point the unit becomes mgC or TgC.

Figure S9 shows the comparison of monthly phytoplankton NPP records derived from CALIOP and MODIS for the southern polar zones. Panels (a) to (e) depict NPP values for different latitudinal bands (40°S–55°S, 55°S–65°S, 65°S–75°S, 75°S–81.5°S, and 81.5°S–45°S). The data demonstrates that CALIOP (blue lines) and MODIS (orange lines) show strong agreement during austral summer, suggesting high consistency between the two datasets. Besides, CALIOP effectively compensates for missing MODIS data during the austral winter, providing a

more continuous and comprehensive NPP record across the entire year.

It is important to acknowledge that by training our model with MODIS data, its inherent biases are propagated into our results. To formally assess this, we identified three primary sources of error contributing to the total uncertainty (E) of our CALIOP-derived products: measurement (M), representation (R), and prediction (P) errors¹²⁹. The total uncertainty can be expressed as the root of the sum of squares of these components: $E = \sqrt{M^2 + R^2 + P^2}$. The measurement error (M) includes the combined uncertainties from the CALIOP input variables and the MODIS reference data used for model training. The representation error (R) arises from spatio-temporal mismatches between observations and the model grid. Following established methods, this error is assumed to be normally distributed with a bias of 0 on a large scale and is not included in the final error budget. The prediction error (P) is the inherent error of our TBTS model, as determined from the validation dataset. Combining these components, the total estimated uncertainty (E) for our CALIOP-derived products (Chla, bbp and Kd) is approximately 30–35%^{43,130}. These uncertainties propagate to the final NPP estimates. As the CbPM is a multiplicative model, the total uncertainty in our NPP estimates (E_{NPP}) can be approximated by the root sum of squares of the uncertainties from our key inputs: $E_{NPP} = \sqrt{E_{Chla}^2 + E_{bbp}^2 + E_{Kd}^2}$. This results in an uncertainty for the final NPP estimate of approximately 55%. It is critical to note that this substantial uncertainty primarily affects the absolute magnitude of our NPP estimates. The central conclusion of our study, however, is the accelerating trend in winter NPP. The calculation of a linear trend is statistically robust against such random errors in individual data points. Our confidence in the positive and significant trend is further bolstered by the consistent increasing trends observed across four different NPP models (Supplementary Fig. S5) and our independent validation using VIIRS data (Supplementary Fig. S10).

Statistical analysis of potential factors and quantitative causality analysis

For the statistical analysis of potential factors influencing Antarctic NPP, we employed a random forest (RF) regression model to quantify the relative contributions of different environmental factors, a method successfully applied for analyzing drivers in environmental science¹³¹. This method allows for the assessment of nonlinear relationships between predictor variables and NPP, providing a robust framework for understanding how various factors such as temperature, salinity, and nutrient availability, influence primary production in the Southern Ocean. To provide a robust and unbiased assessment of feature importance, we used the permutation-based method¹³². This method directly measures a feature's impact on the model's performance on an unseen validation dataset, avoiding the potential biases of standard impurity-based metrics. As originally described by ref. 133, the importance of a single feature is calculated as the average decrease in the model's performance score when the values of that feature are randomly shuffled. This process was repeated multiple times for each feature to ensure statistical stability. The resulting importance values are normalized to ensure that they sum to 100%.

To further explore the causal relationships between Antarctic NPP and various environmental factors, we utilized the PCMCI+ algorithm, which is a powerful statistical method for detecting causal interactions in multivariate time series data^{64,65}. PCMCI+ is a time series causal discovery approach that efficiently identifies causal links by testing for conditional independence between variables¹³⁴. In the method, first, a condition-selection step (PC) is applied to iteratively test for conditional independence and identify the relevant conditions necessary for establishing causal relationships. This step helps reduce the complexity of the model, especially when handling many variables. In the

second step, momentary conditional independence (MCI) tests are performed using a smaller set of selected conditions, helping to address issues such as strong autocorrelation in time series data. Partial correlation (ParCorr) calculations are used for conditional independence testing in this analysis, focusing on linear relationships between variables. The maximum time delay ($\tau_{\max} = 12$) is chosen to reflect teleconnection. The pruning hyperparameter (pc- α) is optimized using the Akaike information criterion (AIC). PCMCI+ produces *p* values for causal links between variables at different time lags, and in this study, links were defined at a strict significance level of 0.05. This approach offers a rigorous way to understand the complex interactions in Antarctic ecosystems and provides insights into how changes in environmental factors influence NPP through direct or mediated pathways. By using PCMCI+, we can identify key drivers of NPP variations that are not merely correlated but have a causal influence, thereby helping to improve our understanding of the underlying mechanisms that regulate primary production in the Southern Ocean.

Data availability

All third-party data used in this study are publicly available from their respective archives. Specifically, MODIS-Aqua Level 3 data were obtained from the NASA Ocean Color Web (<https://oceandata.sci.gsfc.nasa.gov/directdataaccess/Level-3%20Mapped/Aqua-MODIS/>) with an alternative access point at <https://oceandata.sci.gsfc.nasa.gov/l3/>. CALIOP Level-1B and Level-2 products were sourced from the NASA Atmospheric Science Data Center (ASDC) at <https://asdc.larc.nasa.gov/data/CALIPSO/>. In-situ biogeochemical data from BGC-Argo floats are available from the Argo Global Data Assembly Center (<ftp://ftp.ifremer.fr/ifremer/argo/>). Data for sea surface temperature (<https://doi.org/10.48670/moi-00168>), sea surface salinity (<https://doi.org/10.48670/moi-00181>), sea surface wind (<https://doi.org/10.48670/moi-00051>), mixed layer depth (<https://doi.org/10.48670/moi-00052>), and nutrients (<https://doi.org/10.48670/moi-00019>) were obtained from the Copernicus Marine Environment Monitoring Service (CMEMS). Sea ice index data (Version 3) were sourced from the National Snow and Ice Data Center (NSIDC) at <https://doi.org/10.7265/NSK072F8>. The Southern Annular Mode (SAM) index was obtained from the British Antarctic Survey (<https://legacy.bas.ac.uk/met/gjma/sam.html>), and other climate indices were from the NOAA Physical Sciences Laboratory (<https://psl.noaa.gov/data/timeseries/month/>). The processed data generated in this study, including the source data underlying the figures, have been deposited in the CodeOcean database under the identifier <https://doi.org/10.24433/CO.9252735.v1>.

Code availability

The code used for all data processing, analysis, and figure generation in this study is publicly available and fully executable within a CodeOcean capsule, which has been deposited in the Code Ocean repository under accession code 10.24433/CO.9252735.v1 [<https://doi.org/10.24433/CO.9252735.v1>].

References

1. Stirnimann, L. et al. A circum-Antarctic plankton isoscape: carbon export potential across the summertime Southern Ocean. *Glob. Biogeochem. Cycle* **38**, e2023GB007808 (2024).
2. Terrats, L. et al. BioGeoChemical-argo floats reveal stark latitudinal gradient in the Southern Ocean deep carbon flux driven by phytoplankton community composition. *Glob. Biogeochem. Cycle* **37**, e2022GB007624 (2023).
3. Huang, Y., Fassbender, A. ndreaJ. & Bushinsky, S. ethM. Biogenic carbon pool production maintains the Southern Ocean carbon sink. *Proc. Natl. Acad. Sci.* **120**, e2217909120 (2023).
4. Brewin, R. J. W. et al. Ocean carbon from space: current status and priorities for the next decade. *Earth-Sci. Rev.* **240**, 104386 (2023).

5. Thomalla, S. J., Nicholson, S.-A., Ryan-Keogh, T. J. & Smith, M. E. Widespread changes in Southern Ocean phytoplankton blooms linked to climate drivers. *Nat. Clim. Change* **13**, 975–984 (2023).
6. Ryan-Keogh, T. J., Thomalla, S. J., Monteiro, P. M. S. & Tagliabue, A. Multidecadal trend of increasing iron stress in Southern Ocean phytoplankton. *Science* **379**, 834–840 (2023).
7. Haumann, F. A., Gruber, N. & Münnich, M. Sea-ice induced Southern Ocean subsurface warming and surface cooling in a warming climate. *AGU Adv.* **1**, e2019AV000132 (2020).
8. Flexas, M. M., Thompson, A. F., Schodlok, M. P., Zhang, H. & Speer, K. Antarctic Peninsula warming triggers enhanced basal melt rates throughout West Antarctica. *Sci. Adv.* **8**, eabj9134 (2022).
9. Nakayama, Y., Menemenlis, D., Zhang, H., Schodlok, M. & Rignot, E. Origin of circumpolar deep water intruding onto the Amundsen and Bellingshausen sea continental shelves. *Nat. Commun.* **9**, 3403 (2018).
10. Hobbs, W. et al. Observational evidence for a regime shift in summer Antarctic Sea Ice. *J. Clim.* **37**, 2263–2275 (2024).
11. Purich, A. & Doddridge, E. W. Record low Antarctic sea ice coverage indicates a new sea ice state. *Commun. Earth Environ.* **4**, 314 (2023).
12. Raphael, M. N. & Handcock, M. S. A new record minimum for Antarctic sea ice. *Nat. Rev. Earth Environ.* **3**, 215–216 (2022).
13. Henley, S. F. et al. Changing biogeochemistry of the Southern ocean and its ecosystem implications. *Front. Mar. Sci.* **7**, <https://doi.org/10.3389/fmars.2020.00581> (2020).
14. Constable, A. J. et al. Climate change and Southern Ocean ecosystems I: how changes in physical habitats directly affect marine biota. *Glob. Change Biol.* **20**, 3004–3025 (2014).
15. Sallée, J.-B. et al. Summertime increases in upper-ocean stratification and mixed-layer depth. *Nature* **591**, 592–598 (2021).
16. Rozema, P. D. et al. Interannual variability in phytoplankton biomass and species composition in northern Marguerite Bay (West Antarctic Peninsula) is governed by both winter sea ice cover and summer stratification. *Limnol. Oceanogr.* **62**, 235–252 (2017).
17. Deppeler, S. L. & Davidson, A. T. Southern ocean phytoplankton in a changing climate. *Front. Mar. Sci.* **4**, <https://doi.org/10.3389/fmars.2017.00040> (2017).
18. Zhang, Z. et al. Linkage of the physical environments in the northern Antarctic Peninsula region to the Southern Annular Mode and the implications for the phytoplankton production. *Prog. Oceanogr.* **188**, 102416 (2020).
19. Greaves, B. L. et al. The Southern Annular Mode (SAM) influences phytoplankton communities in the seasonal ice zone of the Southern Ocean. *Biogeosciences* **17**, 3815–3835 (2020).
20. Noh, K. M., Lim, H.-G. & Kug, J.-S. Zonally asymmetric phytoplankton response to the Southern annular mode in the marginal sea of the Southern ocean. *Sci. Rep.* **11**, 10266 (2021).
21. Ferreira, A. et al. Climate change is associated with higher phytoplankton biomass and longer blooms in the West Antarctic Peninsula. *Nat. Commun.* **15**, 6536 (2024).
22. Turner, J. S. et al. Changing phytoplankton phenology in the marginal ice zone west of the Antarctic Peninsula. *Mar. Ecol. Prog. Ser.* **734**, 1–21 (2024).
23. Del Castillo, C. E., Signorini, S. R., Karaköylü, E. M. & Rivero-Calle, S. Is the Southern Ocean getting greener?. *Geophys. Res. Lett.* **46**, 6034–6040 (2019).
24. Cael, B. B., Bisson, K., Boss, E., Dutkiewicz, S. & Henson, S. Global climate-change trends detected in indicators of ocean ecology. *Nature* **619**, 551–554 (2023).
25. Duce, R. A. et al. Impacts of atmospheric anthropogenic nitrogen on the open Ocean. *Science* **320**, 893–897 (2008).
26. Riebesell, U. & Gattuso, J.-P. Lessons learned from ocean acidification research. *Nat. Clim. Change* **5**, 12–14 (2015).
27. Yu, S., Bai, Y., He, X., Gong, F. & Li, T. A new merged dataset of global ocean chlorophyll-a concentration for better trend detection. *Front. Mar. Sci.* **10**, <https://doi.org/10.3389/fmars.2023.1051619> (2023).
28. Hoppe, C. J. M. et al. Photosynthetic light requirement near the theoretical minimum detected in Arctic microalgae. *Nat. Commun.* **15**, 7385 (2024).
29. Randelhoff, A. et al. Arctic mid-winter phytoplankton growth revealed by autonomous profilers. *Sci. Adv.* **6**, eabc2678 (2020).
30. Chen, W. et al. Review of airborne oceanic lidar remote sensing. *Intell. Mar. Technol. Syst.* **1**, 10 (2023).
31. Behrenfeld, M. J. et al. Annual boom–bust cycles of polar phytoplankton biomass revealed by space-based lidar. *Nat. Geosci.* **10**, 118–122 (2017).
32. Dierssen, H. M. Hyperspectral measurements, parameterizations, and atmospheric correction of whitecaps and foam from visible to shortwave infrared for ocean color remote sensing. *Front. Earth Sci.* **7**, <https://doi.org/10.3389/feart.2019.00014> (2019).
33. Philibert, R., Waldron, H. & Clark, D. A geographical and seasonal comparison of nitrogen uptake by phytoplankton in the Southern Ocean. *Ocean Sci.* **11**, 251–267 (2015).
34. Arrigo, K. R., van Dijken, G. L. & Bushinsky, S. Primary production in the Southern Ocean, 1997–2006. *J. Geophys. Res.: Oceans* **113**, <https://doi.org/10.1029/2007JC004578> (2008).
35. Ryan-Keogh, T. J., Tagliabue, A. & Thomalla, S. J. Global decline in net primary production underestimated by climate models. *Commun. Earth Environ.* **6**, 75 (2025).
36. Maishal, S. Decadal changes in global oceanic primary productivity and its drivers. *Ocean Land Atmos. Res.* **3**, 0066 (2024).
37. Bisson, K. M. & Cael, B. B. How are under ice phytoplankton related to sea ice in the Southern Ocean?. *Geophys. Res. Lett.* **48**, e2021GL095051 (2021).
38. Ardyna, M. et al. Under-ice phytoplankton blooms: shedding light on the “invisible” part of arctic primary production. *Front. Mar. Sci.* **7**, 2020 (2020).
39. Smith, W. O. Jr. & Zhong, Y. Under-ice mixed layers and the regulation of early spring phytoplankton growth in the Southern Ocean. *Geophys. Res. Lett.* **51**, e2023GL106796 (2024).
40. Zhang, Z. et al. Combining deep learning with physical parameters in POC and PIC inversion from spaceborne lidar CALIOP. *ISPRS J. Photogramm. Remote Sens.* **212**, 193–211 (2024).
41. Zhang, Z. et al. Chlorophyll and POC in polar regions derived from spaceborne lidar. *Front. Mar. Sci.* **10**, <https://doi.org/10.3389/fmars.2023.1050087> (2023).
42. Zhang, S., Chen, P., Zhang, Z. & Pan, D. Carbon air–sea flux in the Arctic Ocean from CALIPSO from 2007 to 2020. *Remote Sens.* **14**, 6196 (2022).
43. Zhang, Z. et al. Retrieving bbp and POC from CALIOP: a deep neural network approach. *Remote Sens. Environ.* **287**, 113482 (2023).
44. Behrenfeld, M. J. et al. Space-based lidar measurements of global ocean carbon stocks. *Geophys. Res. Lett.* **40**, 4355–4360 (2013).
45. Lima, D. T. d. et al. Abiotic changes driving microphytoplankton functional diversity in admiralty Bay, King George Island (Antarctica). *Front. Mar. Sci.* **6**, <https://doi.org/10.3389/fmars.2019.00638> (2019).
46. Taylor, M. H., Losch, M. & Bracher, A. On the drivers of phytoplankton blooms in the Antarctic marginal ice zone: a modeling approach. *J. Geophys. Res.: Oceans* **118**, 63–75 (2013).
47. Haëntjens, N., Boss, E. & Talley, L. D. Revisiting ocean color algorithms for chlorophyll a and particulate organic carbon in the Southern Ocean using biogeochemical floats. *J. Geophys. Res.: Oceans* **122**, 6583–6593 (2017).
48. Bisson, K. M. et al. Seasonal bias in global ocean color observations. *Appl. Opt.* **60**, 6978–6988 (2021).

49. Yang, B. et al. In Situ estimates of net primary production in the Western North Atlantic with argo profiling floats. *J. Geophys. Res. Biogeosci.* **126**, e2020JG006116 (2021).
50. Jena, B. et al. Evolution of Antarctic Sea ice ahead of the record low annual maximum extent in september 2023. *Geophys. Res. Lett.* **51**, e2023GL107561 (2024).
51. Irwin, A. J. & Finkel, Z. V. Mining a sea of data: deducing the environmental controls of ocean chlorophyll. *PLoS One* **3**, e3836 (2008).
52. Lheureux, A. et al. Bi-decadal variability in physico-biochemical characteristics of temperate coastal ecosystems: from large-scale to local drivers. *Mar. Ecol. Prog. Ser.* **660**, 19–35 (2021).
53. Feng, J., Li, D., Zhang, J. & Zhao, L. Variations in and environmental controls of primary productivity in the Amundsen Sea. *Biogeosci. Discuss.* **2021**, 1–44 (2021).
54. Gholizadeh, M. H., Melesse, A. M. & Reddi, L. A comprehensive review on water quality parameters estimation using remote sensing techniques. *Sensors* **16**, 1298 (2016).
55. Ellison, E., Mazloff, M. & Mashayek, A. The rapid response of southern ocean biological productivity to changes in background small scale turbulence. *J. Geophys. Res.: Oceans* **129**, e2024JC021158 (2024).
56. Flynn, R. F. et al. Summertime productivity and carbon export potential in the Weddell Sea, with a focus on the waters adjacent to Larsen C Ice Shelf. *Biogeosciences* **18**, 6031–6059 (2021).
57. Smith Jr., W. O. & Comiso, J. C. Influence of sea ice on primary production in the Southern Ocean: a satellite perspective. *J. Geophys. Res.: Oceans* **113**, <https://doi.org/10.1029/2007JC004251> (2008).
58. Kumar, A., Dwivedi, S. & Rajak, D. R. Ocean sea-ice modelling in the Southern Ocean around Indian Antarctic stations. *J. Earth Syst. Sci.* **126**, 70 (2017).
59. Moore, C. M. et al. Processes and patterns of oceanic nutrient limitation. *Nat. Geosci.* **6**, 701–710 (2013).
60. Alderkamp, A. C., Baar, H. J. W. D., Visser, C. R. J. W. & Arrigoa, K. R. Can photoinhibition control phytoplankton abundance in deeply mixed water columns of the Southern Ocean?. *Limnol. Oceanogr.* **55**, 1248–1264 (2010).
61. Boyd, P. W. et al. Marine phytoplankton temperature versus growth responses from polar to tropical waters – outcome of a scientific community-wide study. *PLoS One* **8**, e63091 (2013).
62. Hague, M. & Vichi, M. Southern Ocean biogeochemical argo detect under-ice phytoplankton growth before sea ice retreat. *Biogeosciences* **18**, 25–38 (2021).
63. Marshall, G. J. Trends in the Southern Annular mode from observations and reanalyses. *J. Clim.* **16**, 4134–4143 (2003).
64. Nowack, P., Runge, J., Eyring, V. & Haigh, J. D. Causal networks for climate model evaluation and constrained projections. *Nat. Commun.* **11**, 1415 (2020).
65. Krich, C. et al. Estimating causal networks in biosphere–atmosphere interaction with the PCMCi approach. *Biogeosciences* **17**, 1033–1061 (2020).
66. Lenton, A. & Matear, R. J. Role of the southern annular mode (SAM) in Southern Ocean CO₂ uptake. *Glob. Biogeochem. Cycle* **21**, <https://doi.org/10.1029/2006GB002714> (2007).
67. Perren, B. B. et al. Southward migration of the Southern Hemisphere westerly winds corresponds with warming climate over centennial timescales. *Commun. Earth Environ.* **1**, 58 (2020).
68. Boschat, G., Purich, A., Rudeva, I. & Arblaster, J. Impact of zonal and meridional atmospheric flow on surface climate and extremes in the Southern Hemisphere. *J. Clim.* **36**, 5041–5061 (2023).
69. Verfaillie, D. et al. The circum-Antarctic ice-shelves respond to a more positive Southern Annular mode with regionally varied melting. *Commun. Earth Environ.* **3**, 139 (2022).
70. Morioka, Y. et al. Antarctic sea ice multidecadal variability triggered by Southern Annular Mode and deep convection. *Commun. Earth Environ.* **5**, 633 (2024).
71. Screen, J. A., Gillett, N. P., Karpechko, A. Y. & Stevens, D. P. Mixed layer temperature response to the Southern annular mode: mechanisms and model representation. *J. Clim.* **23**, 664–678 (2010).
72. Sen Gupta, A. & England, M. H. Coupled ocean–atmosphere–ice response to variations in the Southern annular mode. *J. Clim.* **19**, 4457–4486 (2006).
73. Yuan, X. ENSO-related impacts on Antarctic sea ice: a synthesis of phenomenon and mechanisms. *Antarct. Sci.* **16**, 415–425 (2004).
74. Dou, J. & Zhang, R. Impact of sea surface temperature in the extratropical southern Indian Ocean on Antarctic Sea Ice in Austral spring. *J. Clim.* **36**, 8259–8275 (2023).
75. Dou, J. & Zhang, R. Weakened relationship between ENSO and Antarctic sea ice in recent decades. *Clim. Dyn.* **60**, 1313–1327 (2023).
76. Buchovecky, B. et al. Potential predictability of the spring bloom in the Southern Ocean Sea ice zone. *Geophys Res Lett.* **50**, e2023GL105139 (2023).
77. Arteaga, L. A., Boss, E., Behrenfeld, M. J., Westberry, T. K. & Sarmiento, J. L. Seasonal modulation of phytoplankton biomass in the Southern Ocean. *Nat. Commun.* **11**, 5364 (2020).
78. Horvat, C., Bisson, K., Seabrook, S., Cristi, A. & Matthes, L. C. Evidence of phytoplankton blooms under Antarctic sea ice. *Front. Mar. Sci.* **9**, <https://doi.org/10.3389/fmars.2022.942799> (2022).
79. Meredith, M. P. Carbon storage shifts around Antarctica. *Nat. Commun.* **13**, 3400 (2022).
80. Hauck, J. et al. On the Southern Ocean CO₂ uptake and the role of the biological carbon pump in the 21st century. *Glob. Biogeochem. Cycle* **29**, 1451–1470 (2015).
81. Shadwick, E. H. et al. Sea ice suppression of CO₂ outgassing in the West Antarctic Peninsula: implications for the evolving Southern Ocean carbon sink. *Geophys. Res. Lett.* **48**, e2020GL091835 (2021).
82. Sørdeide, J. E., Leu, E. V., Berge, J., Graeve, M. & Falk-Petersen, S. Timing of blooms, algal food quality and *Calanus glacialis* reproduction and growth in a changing Arctic. *Glob. change Biol.* **16**, 3154–3163 (2010).
83. Anderson, M. A. et al. Changing environmental conditions have altered the feeding ecology of two keystone Arctic marine predators. *Sci. Rep.* **13**, 14056 (2023).
84. Tréguer, P. et al. Influence of diatom diversity on the ocean biological carbon pump. *Nat. Geosci.* **11**, 27–37 (2018).
85. Cermeño, P. et al. The role of nutricline depth in regulating the ocean carbon cycle. *Proc. Natl. Acad. Sci.* **105**, 20344–20349 (2008).
86. Svensen, C. et al. Zooplankton communities associated with new and regenerated primary production in the Atlantic Inflow North of Svalbard. *Front. Mar. Sci.* **6**, 2019 (2019).
87. Smith, S. V. & Gattuso, J.-P. Balancing the oceanic calcium carbonate cycle: consequences of variable water column Ψ . *Aquat. Geochem.* **17**, 327–337 (2011).
88. Riebesell, U., Körtzinger, A. & Oschlies, A. Sensitivities of marine carbon fluxes to ocean change. *Proc. Natl. Acad. Sci.* **106**, 20602–20609 (2009).
89. Krumhardt, K. M., Lovenduski, N. S., Freeman, N. M. & Bates, N. R. Apparent increase in coccolithophore abundance in the subtropical North Atlantic from 1990 to 2014. *Biogeosciences* **13**, 1163–1177 (2016).
90. Shutler, J. D. et al. Coccolithophore surface distributions in the North Atlantic and their modulation of the air–sea flux of CO₂ from 10 years of satellite Earth observation data. *Biogeosciences* **10**, 2699–2709 (2013).

91. Castro de la Guardia, L. et al. Assessing the role of high-frequency winds and sea ice loss on arctic phytoplankton blooms in an ice-ocean-biogeochemical model. *J. Geophys. Res. Biogeosci.* **124**, 2728–2750 (2019).
92. Knoll, L. B., Fry, B., Hayes, N. M. & Sauer, H. M. Reduced snow and increased nutrients show enhanced ice-associated photoautotrophic growth using a modified experimental under-ice design. *Limnol. Oceanogr.* **69**, 203–216 (2024).
93. Barber, D. G. et al. Consequences of change and variability in sea ice on marine ecosystem and biogeochemical processes during the 2007–2008 Canadian International Polar Year program. *Clim. Change* **115**, 135–159 (2012).
94. Wang, J. et al. The impacts of combined SAM and ENSO on seasonal Antarctic sea ice changes. *J. Clim.* **36**, 3553–3569 (2023).
95. Risaro, D. B., Chidichimo, M. P. & Piola, A. R. Interannual variability and trends of sea surface temperature around Southern South America. *Front. Mar. Sci.* **9**, <https://doi.org/10.3389/fmars.2022.829144> (2022).
96. Kim, H. & Ducklow, H. W. A Decadal (2002–2014) analysis for dynamics of heterotrophic bacteria in an Antarctic Coastal ecosystem: variability and physical and biogeochemical forcings. *Front. Mar. Sci.* **3**, <https://doi.org/10.3389/fmars.2016.00214> (2016).
97. Meredith, M. P. & King, J. C. Rapid climate change in the ocean west of the Antarctic Peninsula during the second half of the 20th century. *Geophys. Res. Lett.* **32**, <https://doi.org/10.1029/2005GL024042> (2005).
98. Biggs, T. E. G. et al. Control of Antarctic phytoplankton community composition and standing stock by light availability. *Polar Biol.* **45**, 1635–1653 (2022).
99. Getzewich, B. J. et al. CALIPSO lidar calibration at 532nm: version 4 daytime algorithm. *Atmos. Meas. Tech.* **11**, 6309–6326 (2018).
100. Wong, A. P. S. et al. Argo data 1999–2019: two million temperature-salinity profiles and subsurface velocity observations from a global array of profiling floats. *Front. Mar. Sci.* **7**, <https://doi.org/10.3389/fmars.2020.00700> (2020).
101. Claustre, H., Johnson, K. S. & Takeshita, Y. Observing the global ocean with biogeochemical-argo. *Annu. Rev. Mar. Sci.* **12**, 23–48 (2020).
102. Johnson, K. & Claustre, H. Bringing biogeochemistry into the Argo age. *Eos, Transactions American Geophysical Union*, <https://doi.org/10.1029/2016EO062427> (2016).
103. Good, S. et al. The current configuration of the OSTIA system for operational production of foundation sea surface temperature and ice concentration analyses. *Remote Sens.* **12**, 720 (2020).
104. Droghei, R., Buongiorno Nardelli, B. & Santoleri, R. A new global sea surface salinity and density dataset from multivariate observations (1993–2016). *Front. Mar. Sci.* **5**, <https://doi.org/10.3389/fmars.2018.00084> (2018).
105. Droghei, R., Nardelli, B. B. & Santoleri, R. Combining in situ and satellite observations to retrieve salinity and density at the ocean surface. *J. Atmos. Ocean. Technol.* **33**, 1211–1223 (2016).
106. Buongiorno Nardelli, B., Droghei, R. & Santoleri, R. Multi-dimensional interpolation of SMOS sea surface salinity with surface temperature and in situ salinity data. *Remote Sens. Environ.* **180**, 392–402 (2016).
107. Mulet, S., Rio, M. H., Mignot, A., Guinehut, S. & Morrow, R. A new estimate of the global 3D geostrophic ocean circulation based on satellite data and in-situ measurements. *Deep Sea Res. Part II* **77–80**, 70–81 (2012).
108. Guinehut, S., Dhomp, A. L., Larnicol, G. & Le Traon, P. Y. High resolution 3-D temperature and salinity fields derived from in situ and satellite observations. *Ocean Sci.* **8**, 845–857 (2012).
109. Fetterer, F., Knowles, K., Meier, W., Savoie, M. & Windnagel, A. (NSIDC, 2017).
110. Rayner, N. A. et al. Global analyses of sea surface temperature, sea ice, and night marine air temperature since the late nineteenth century. *J. Geophys. Res. Atmos.* **108**, <https://doi.org/10.1029/2002JD002670> (2003).
111. Ropelewski, C. F. & Jones, P. D. An extension of the Tahiti–Darwin Southern Oscillation Index. *Mon. Weather Rev.* **115**, 2161–2165 (1987).
112. Mantua, N. J., Hare, S. R., Zhang, Y., Wallace, J. M. & Francis, R. C. A Pacific interdecadal climate oscillation with impacts on salmon production*. *Bull. Am. Meteorol. Soc.* **78**, 1069–1080 (1997).
113. Saji, N. H. & Yamagata, T. Possible impacts of Indian Ocean Dipole mode events on global climate. *Clim. Res.* **25**, 151–169 (2003).
114. Winker, D. M. et al. Overview of the CALIPSO mission and CALIOP data processing algorithms. *J. Atmos. Ocean. Technol.* **26**, 2310–2323 (2009).
115. Lu, X. et al. Enabling value added scientific applications of ICESat-2 data with effective removal of afterpulses. *Earth Space Sci.* **8**, e2021EA001729 (2021).
116. Lu, X., Hu, Y., Trepte, C., Zeng, S. & Churnside, J. H. Ocean subsurface studies with the CALIPSO spaceborne lidar. *J. Geophys. Res. Oceans* **119**, 4305–4317 (2014).
117. Lu, X. et al. New Ocean Subsurface optical properties from space lidars: CALIOP/CALIPSO and ATLAS/ICESat-2. *Earth Space Sci.* **8**, e2021EA001839 (2021).
118. Dionisi, D., Brando, V. E., Volpe, G., Colella, S. & Santoleri, R. Seasonal distributions of ocean particulate optical properties from spaceborne lidar measurements in Mediterranean and Black sea. *Remote Sens. Environ.* **247**, 111889 (2020).
119. Hu, Y. et al. Sea surface wind speed estimation from space-based lidar measurements. *Atmos. Chem. Phys.* **8**, 3593–3601 (2008).
120. Kong, Q. et al. Combining deep learning with physics based features in explosion-earthquake discrimination. *Geophys. Res. Lett.* **49**, e2022GL098645 (2022).
121. LeCun, Y., Bengio, Y. & Hinton, G. Deep learning. *Nature* **521**, 436–444 (2015).
122. Hinton, G., Srivastava, N. & Swersky, K. Overview of mini-batch gradient descent. *Neural Networks for Machine Learning* **575** (2012).
123. Takahashi, T. et al. Climatological mean and decadal change in surface ocean pCO₂, and net sea–air CO₂ flux over the global oceans. *Deep Sea Res. Part II* **56**, 554–577 (2009).
124. Denvil-Sommer, A., Gehlen, M., Vrac, M. & Mejia, C. LSCE-FFNN-v1: a two-step neural network model for the reconstruction of surface ocean pCO₂ over the global ocean. *Geosci. Model Dev.* **12**, 2091–2105 (2019).
125. Zhang, Z. et al. Consistency analysis of water diffuse attenuation between ICESat-2 and MODIS in marginal sea: a case study in China Sea. *Remote Sens. Environ.* **318**, 114602 (2025).
126. Werdell, P. J. & Bailey, S. W. An improved in-situ bio-optical data set for ocean color algorithm development and satellite data product validation. *Remote Sens. Environ.* **98**, 122–140 (2005).
127. Westberry, T., Behrenfeld, M. J., Siegel, D. A. & Boss, E. Carbon-based primary productivity modeling with vertically resolved photoacclimation. *Glob. Biogeochem. Cycle* **22**, <https://doi.org/10.1029/2007GB003078> (2008).
128. Behrenfeld, M. J., Boss, E., Siegel, D. A. & Shea, D. M. Carbon-based ocean productivity and phytoplankton physiology from space. *Glob. Biogeochem. Cycle* **19**, <https://doi.org/10.1029/2004GB002299> (2005).
129. Gregor, L. & Gruber, N. OceanSODA-ETHZ: a global gridded data set of the surface ocean carbonate system for seasonal to decadal studies of ocean acidification. *Earth Syst. Sci. Data* **13**, 777–808 (2021).
130. Zhang, Z. et al. Chlorophyll and POC in polar regions derived from spaceborne lidar. *Front. Mar. Sci.* **10**, 2023 (2023).

131. Liu, D. et al. Substantial increase of organic carbon storage in Chinese lakes. *Nat. Commun.* **15**, 8049 (2024).
132. Gregorutti, B., Michel, B. & Saint-Pierre, P. Correlation and variable importance in random forests. *Stat. Comput.* **27**, 659–678 (2017).
133. Breiman, L. Random forests. *Mach. Learn.* **45**, 5–32 (2001).
134. Runge, J., Nowack, P., Kretschmer, M., Flaxman, S. & Sejdinovic, D. Detecting and quantifying causal associations in large nonlinear time series datasets. *Sci. Adv.* **5**, eaau4996 (2019).

Acknowledgements

We gratefully acknowledge the NASA Ocean Biology Processing Group (OBPG) for maintaining and distributing MODIS products and biogeochemical-Argo data from the Argo Data Assembly Center. We thank GDAC for providing Argo data. These data were collected and made freely available by the International Argo Program and the national programs that contribute to it. (<https://argo.ucsd.edu>, <https://www.ocean-ops.org>). The Argo Program is part of the Global Ocean Observing System. This study has been conducted using E.U. Copernicus Marine Service Information; <https://doi.org/10.48670/moi-00168>; <https://doi.org/10.48670/moi-00051>; <https://doi.org/10.48670/moi-00181>; <https://doi.org/10.48670/moi-00052>; <https://doi.org/10.48670/moi-00019>. This study was supported by the National Natural Science Foundation of China (Grant #42322606, P.C.; Grant #42276180, P.C.; Grant #W2521002, P.C.), Zhejiang Provincial Natural Science Foundation (Grant # LZ25D060001, P.C.), National Key Research and Development Program of China (Grant #2022YFB3901703, P.C.; Grant #2022YFB3902603, P.C.).

Author contributions

P.C. and Z.Z. conceived the study and prepared the original manuscript. Z.Z., S.Z., and D.P. provided parts of the data. K.B., C.J., P.G., D.D., and Y.H. prepared and/or revised the manuscript.

Competing interests

The authors declare no competing interests.

Additional information

Supplementary information The online version contains supplementary material available at <https://doi.org/10.1038/s41467-025-66275-w>.

Correspondence and requests for materials should be addressed to Peng Chen or Siqi Zhang.

Peer review information *Nature Communications* thanks S. Lan Smith and the other anonymous reviewer(s) for their contribution to the peer review of this work. A peer review file is available.

Reprints and permissions information is available at <http://www.nature.com/reprints>

Publisher's note Springer Nature remains neutral with regard to jurisdictional claims in published maps and institutional affiliations.

Open Access This article is licensed under a Creative Commons Attribution-NonCommercial-NoDerivatives 4.0 International License, which permits any non-commercial use, sharing, distribution and reproduction in any medium or format, as long as you give appropriate credit to the original author(s) and the source, provide a link to the Creative Commons licence, and indicate if you modified the licensed material. You do not have permission under this licence to share adapted material derived from this article or parts of it. The images or other third party material in this article are included in the article's Creative Commons licence, unless indicated otherwise in a credit line to the material. If material is not included in the article's Creative Commons licence and your intended use is not permitted by statutory regulation or exceeds the permitted use, you will need to obtain permission directly from the copyright holder. To view a copy of this licence, visit <http://creativecommons.org/licenses/by-nc-nd/4.0/>.

© The Author(s) 2025